Forschungszentrum Karlsruhe

in der Helmholtz-Gemeinschaft

Wissenschaftliche Berichte

FZKA 6756

The Karlsruhe Dynamo Experiment

U. Müller, R. Stieglitz, S. Horanyi*

Institut für Kern- und Energietechnik

*Permanent address:
KFKI Atomic Energy Research Institute
Budapest / Hungary

Forschungszentrum Karlsruhe GmbH, Karlsruhe

2002

Impressum der Print-Ausgabe:

Als Manuskript gedruckt

Forschungszentrum Karlsruhe GmbH
Postfach 3640, 76021 Karlsruhe

Mitglied der Hermann von Helmholtz-Gemeinschaft
Deutscher Forschungszentren (HGF)

ISSN 0947-8620

Abstract

The Karlsruhe Dynamo experiment is aimed at showing that a liquid sodium flow in an array of columnar helical vortices, confined in a cylindrical container, can generate a magnetic field by self-excitation. The flow structures in the liquid core of the Earth are topologically comparable to those being realized within the Karlsruhe test module.

In three test series it has been demonstrated that magnetic self-excitation occurs and a permanent magnetic saturation field develops which oscillates about a well defined mean value for fixed flow rates. Dynamo action is observed as an imperfect bifurcation from a seed magnetic field of the environment. Two quasi-dipolar magnetic fields of opposite direction have been realized. A transition between these two states can be enforced through an imposition of a sufficiently strong external magnetic perturbation on the initially existent dynamo field. These perturbations were induced with the aid of two Helmholtz coils.

A time series analysis of the magnetic field fluctuations shows several characteristic dynamic features which are in agreement with theoretical predictions of models available in the literature.

Das Karlsruher Dynamoexperiment

Zusammenfassung

Das Karlsruher Dynamoexperiment hat gezeigt, dass ein Feld säulenartiger, gegensinnig rotierender Stömungswirbel in einem mit flüssigem Natrium gefülltem Zylinder ein dauerhaftes magnetisches Feld durch Selbsterregung erzeugen kann. Das im Karlsruher Experiment erzeugte Strömungsmuster hat gewisse topologische Ähnlichkeit mit dem im flüssigen Erdkern.

In drei bisher durchgeführten Versuchsreihen erschien beim Überschreiten einer kritischen Strömungsgeschwindigkeit ein Magnetfeld durch Selbsterregung. Beim Überschreiten der kritischen Strömungszustände entwickelte sich ein permanentes, gesättigtes Magnetfeld mit signifikanter Intensität, das um einen definierten Mittelwert oszillierte. Im Experiment stellte sich die magnetische Selbsterregung als imperfekte Verzweigung ein, die sich aus einem Streufeld heraus entwickelte. Es konnten zwei magnetische Dipolfelder mit entgegengesetzter Richtung realisiert werden. Der Übergang zwischen den beiden Zuständen wurde durch ein mit Hilfe externer Helmholtzspulen generiertes Magnetfeld erzwungen, das dem selbsterregten Magnetfeld überlagert wurde.

Eine Analyse der Zeitreihensignale der Magnetfeldfluktuationen hat mehrere charakteristische dynamische Eigenschaften aufgezeigt, die im großen und ganzen mit aus der Literatur bekannten Modellvorstellungen in Einklang stehen.

TABLE OF CONTENT

1 Introduction

Mechanical systems capable of converting mechanical into electromagnetic energy are called dynamos. Technical dynamos are utilized for electricity generation in our industrialized civilization. In principle these power generators are constructed in a complex way using multiply-connected copper wiring arranged in several coils combined with ferromagnetic material which rotate relatively to each other in such a way that self-excitation of an electro-dynamic state occurs. A detailed description of a technical dynamo can be found in any textbook of fundamental and applied physics. These dynamos in multiply-connected material systems are to be distinguished from homogeneous dynamos which in principle originate from vortical flows in electrically conducting homogeneous fluids contained in singly-connected domains where the fluid flow may be driven by external or internal forces. The existence of such homogeneous hydromagnetic dynamos is not obvious, as any induced current in the homogeneous conductor may short circuit and vanish from the conductor without amplifying a seed magnetic field which together with the fluid motion generated the current.

The investigation of homogeneous dynamos has received much attention in geo- and astrophysics during the last fifty years, as it is generally accepted today that the origin of observed planetary-, solar- and even galactic magnetic fields is dynamo action in the interior of these celestial bodies or "clouds". The historic development and the present state of the art can be obtained from numerous survey articles on this subject (see e.g. Busse (1978, 2000), Rittinghouse Inglis (1981), Rädler (1995), Moss (1997), Glatzmaier & Roberts (2000), Müller & Stieglitz (2002)). The vast majority of the performed research has been focused on theory of homogeneous dynamos. Only recently a number of experimental research programs have been initiated to demonstrate homogeneous dynamo action in the laboratory. So far only in two laboratories, at the Physics Institute in Riga and at the Forschungszentrum Karlsruhe, dynamo actions has been successfully realised in an experiment (see Gailitis et al.(2001), Stieglitz & Müller (2001) and for further information on this subject the survey of experimental activities by Müller & Stieglitz 2002)).

In this article we report the results of hydrodynamic dynamo experiments performed at the Institut fuer Kern- und Energietechnik (IKET) of the Forschungszentrum Karlsruhe. The article is organized as follows: Chapter 2 outlines a theoretical dynamo model for the experiment. Chapter 3 describes the experimental set-up and the measuring techniques being used. The experimental results are presented in chapter 4. Finally, in chapter 5 experimental and theoretical results are compared and discussed. Chapter 6 draws some conclusions and gives perspectives.

2 The theoretical background

2.1 General aspects

It is generally accepted today that planetary dynamos are driven by buoyant convection in the liquid and electrically well conducting core of celestial bodies. A general description of the dynamo process requires the solution of the complete set of coupled thermo-fluiddynamic and electro-magnetic transport equations in finite, e.g. spherical domains together with appropriate boundary conditions. This is a formidable mathematical problem which only recently has been tackled with some success by several research groups utilizing advanced methods of Computational Fluid Mechanics (CFD). A summary of the state of the art of the numerical approach of the convection-driven geodynamo problem is given by Jones (2000), Busse (2000), Glatzmaier & Roberts (2000).

In the past the thermo-fluiddynamic and the magneto-hydrodynamic aspects of the planetary dynamo problem have often been considered separately in order to reduce the complexity of the overall problem to mathematically treatable or experimentally accessible subtasks.

From numerous theoretical and experimental investigations on buoyant convection in rapidly rotating spheres or spherical shells a convincing picture of the coherent flow structures in the liquid core of rotating planets has emerged (see e.g. Busse (1971, 1992), Carrigan & Busse (1974, 1976, 1983), Zhang (1992)). A characteristic feature of the internal, buoyancy driven flow in major planets is an assembly of large columnar vortices with axes parallel to the planet's axis of rotation. These vortices are of the Taylor-Proudman type in the near equator range and of the Bénard type in the pole regions. This is sketched in figure 2.1, but the details will not be further discussed here, as we shall focus in this article on the magnetohydrodynamic aspects of planetary dynamos. With regard to the origin of the vortex flow we refer to the literature for more details.

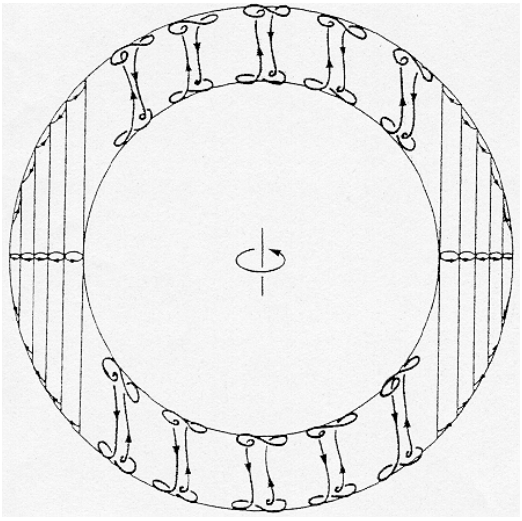

Figure 2.1 Columnar vortex pattern of buoyancy driven convection in a rapidly rotating spherical shell after Busse (1994).

The associated hydromagnetic dynamo problem starts from the assumption that the velocity field is known or can be directly calculated from a given pressure or conservative force distribution. This reduced problem has recently been reformulated by Tilgner & Busse (2002). It is governed by the following set of dimensionless equations for the velocity $\mathbf{u}$ the pressure p and the magnetic induction $\mathbf{B}$

$$\partial_t \mathbf{u} + (\mathbf{u}\cdot\nabla)\mathbf{u} = -\nabla p + \frac{1}{Re}\nabla^2 \mathbf{u} + (\nabla\times\mathbf{B})\times\mathbf{B} + \mathbf{f}, \tag{2.1a}$$

$$\nabla\cdot \mathbf{u} = 0, \tag{2.1b}$$

$$\partial_t \mathbf{B} + \nabla\times(\mathbf{B}\times\mathbf{u}) = \frac{1}{Rm}\nabla^2 \mathbf{B}, \tag{2.1c}$$

$$\nabla\cdot \mathbf{B} = 0. \tag{2.1d}$$

Here the hydrodynamic and magnetic Reynolds numbers (Re, Rm) are defined as

$$Re = \frac{U_o d}{\nu}, \quad Rm = \frac{U_o d}{\lambda}, \tag{2.2}$$

where U_0 is a reference velocity, d a characteristic dimension of the velocity and magnetic field and ν and λ are the viscous and the magnetic diffusivities. The reference velocity U_0 may be defined by the volumetric flow rate $\dot{V}$ in the laboratory model and a particular flow cross-section. Aside from the pressure p a forcing function $\mathbf{f}$ has been introduced in order to simulate specific velocity distributions of laboratory dynamos.

2.2 Linear theory for onset of dynamo action

If the onset of dynamo action is of primary interest, the model equations 2.1 can be simplified further by considering perfect fluids with conservative body forces and neglecting the coupling Lorentz forces $(\nabla x\mathbf{B})x\mathbf{B}$, since they are small of second order in $|\mathbf{B}|$. Among others there is a whole class of steady solutions for velocity fields, called Beltrami flows, which satisfy the condition $\mathbf{u}\,x(\nabla x\,\mathbf{u})=0$ and which can easily be constructed for plane, cylindrical and spherical geometries (see Pekeris et al. (1973)). These solutions may be introduced into equation 2.1c. Together with boundary conditions for the magnetic field at the surface of the flow domain equations 2.1c and 2.1d define a so-called kinematic dynamo problem. A solution of this problem can be obtained in form of a complex product function

$$\mathbf{B}(x,t) = exp(\gamma\, t)\cdot\mathbf{b}(x), \tag{2.3}$$

where the growth rate γ is determined by the associated boundary eigenvalue problem. For $R(\gamma) > 0$ self-excitation of the magnetic field i.e. dynamo action occurs; for $R(\gamma) < 0$ any initially given seed magnetic field decays in time. Naturally, the growth rate depends on the magnetic Reynolds number Rm and the structure of the velocity field.

With regard to the anticipated quasi-regular vortical flow structure in the liquid core of a planet (see figure 2.1) it is of particular interest to investigate the potential for dynamo action of periodic velocity fields. This was done first in a general form by Childress (1967, 1970) and Roberts (1970, 1972) for infinitely extended fields. They proved mathematically that dynamos exist "for almost all steady spatially periodic motions of a homogeneous conducting fluid at almost all values of the conductivity." Moreover, Childress (1967) derived an existence proof for magnetic self-excitation in a spherical liquid conductor containing a quasi-periodic velocity distribution. The proof is constructive and is based on the presumption of scale separation between the period length L and the radius of the sphere R. Gailitis (1967) elaborated an analytical solution of this problem using the “Mean Field Theory” of Steenbeck et al. (1966). He shows that in liquid sodium and for geometrical dimensions of *1m* for the sphere and *0.1m* for the velocity period the velocity should be of the order of $|\mathbf{v}| \approx 1m/s$ to achieve self-excitation. Furthermore, he concludes from the current distribution that a cylindrical confinement of the periodic velocity field would be more favourable for dynamo action at low velocities i.e. at low magnetic Reynolds numbers. Busse (1992) derived an approximate solution for the kinematic dynamo problem for a periodic velocity field in a cylindrical confinement. He started from a Roberts' type velocity distribution in the form

$$\mathbf{v}=(A\sqrt{2}\,\sin\frac{\pi}{a}x\cdot\cos\frac{\pi}{a}y,\,-A\sqrt{2}\cos\frac{\pi}{a}x\cdot\sin\frac{\pi}{a}y,\,C\sin\frac{\pi}{a}x\cdot\sin\frac{\pi}{a}y). \tag{2.4}$$

A pattern of this velocity distribution is sketched in figure 2.2a.In his analysis he assumed that the period length $L=2a$ is much smaller than the cylinder radius r_0 and its height d and that the only boundary condition at the cylinder surface S is a vanishing normal component of the mean electric current density **j** which gives

$$\mathbf{j}\cdot\mathbf{n}=\frac{1}{Rm}(\nabla\times\mathbf{B})\cdot\mathbf{n}=0 \qquad \text{on} \quad S, \tag{2.5}$$

where **n** is the unit normal vector on the cylinder surface. In terms of magnetic Reynolds numbers and geometrical scales he obtains a condition for dynamo action in the form

$$Rm_H\cdot Rm_C \geq \frac{16}{\pi}\frac{a}{d}\left[1+\left(\frac{3.83}{\pi}\frac{d}{r_o}\right)^2\right]. \tag{2.6}$$

In a slight modification of the original formulation of Busse and with regard to the forth-coming explanations we have introduced here Reynolds numbers based on the volumetric flow rates of the axial and azimuthal velocity components in an individual flow cell (see figure 2.2a) and the relevant length scales as $Rm_C=\dot{V}_C/(a\cdot\lambda)$, $Rm_H=\dot{V}_H/(h\cdot\lambda)$ with λ as the magnetic diffusivity and h the helical pitch (see figure 3.1b). (It must be mentioned here that relationship (2.6) is not suitable for a direct comparison with the experimental results in chapter 5, as it was derived for an axisymmetric magnetic field. Therefore, it is not further discussed). Busse (1992) proposed to demonstrate the feasibility of a homogeneous dynamo in the laboratory and to design an experiment according to his model conception which is sketched in figure 2.2b. With regard to the coherent and quasi-periodic columnar vortex

structures there is some similarity between the conjectured flow pattern in the liquid core of fast rotating planets and the suggested laboratory model. However, Busse's original model is affected with an unrealistic feature, as it implicates, due to the simplified boundary condition for the current density, a quasi-periodic continuation of the magnetic field to the outside of the cylinder.

For laboratory application the model has been decisively improved by Tilgner (1997), and Rädler et al. (1996, 1998). These authors embedded the cylinder, containing the arrangement of counter rotating helical vortices, into a sphere containing the same conducting material inside but being bounded by vacuum to the outside (see figure 2.2c). This requires that equations 2.1c and d must be solved inside the cylinder. In the spherical sections of stagnant fluid and in the outside domain Ampere's equation 2.1c has to be satisfied together with equation 2.1d for $\upsilon = 0$ and with appropriate matching conditions for the current density and the magnetic field at the interfaces. Tilgner (1997) used a spectral method to determine numerically the amplification rates and the mode of the magnetic field under conditions of self-excitation. In particular he derived conditions for the marginal state i.e. for the case of zero amplification in terms of helical and axial flow rates. Rädler et al. (1996,1998) applied the Mean Field Theory to solve the eigenvalue problem associated with the amplification rate of dynamo action. Tilgner (1997) as well as Rädler et al. (1996) predict similar results for the structure of the magnetic field and the dependency of the amplification rate on the magnetic Reynolds numbers and the volumetric flow rates respectively. The non-axisymmetric mode with an azimuthal order number $m=1$ shows the largest amplification for all combinations of magnetic Reynolds numbers. The mean magnetic field has a spiral stair case structure in the near field and a dipolar orientation perpendicular to the cylinder axis in the far distance.

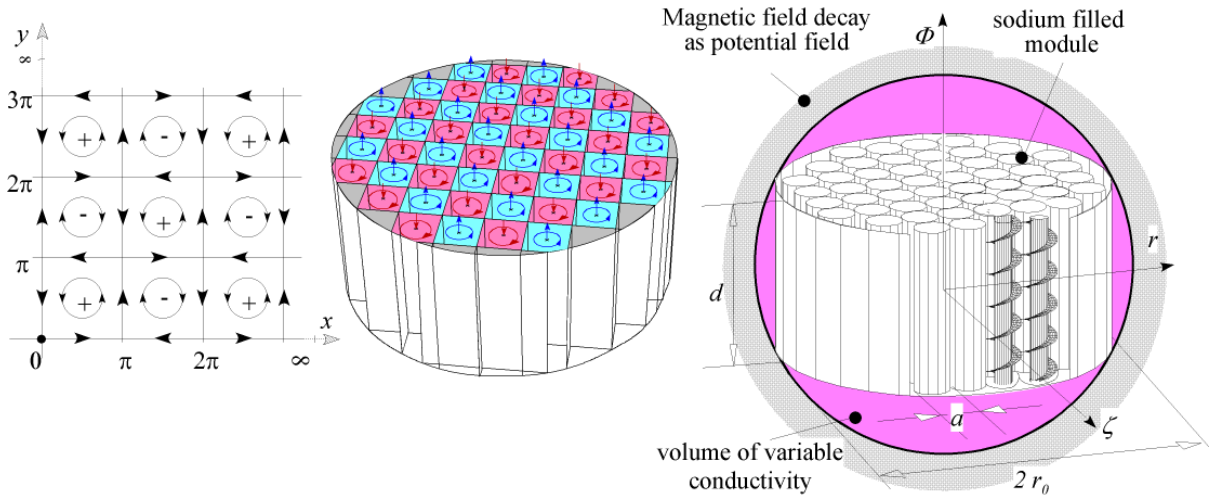

Figure 2.2: a) Non-confined periodic vortex pattern after Roberts (1972) and in modified form after Busse (1992); b) Busse's vortex arrangement confined in a cylindrical domain; c) Tilgner's (1997) and Apel et al. (1996) vortex arrangement in a sphere.

2.3 The nonlinear saturated dynamo states

An interesting aspect of the hydrodynamic dynamo beyond the marginal state (which we shall denote further as "critical" state) is the hydromagnetic mechanism which leads to a saturated magnetic state. The saturation effect is principally caused by the feedback of the Lorentz forces $\mathbf{f}_L = \mathbf{j} \times \mathbf{B}$ on the velocity field described by equation 2.1a. For liquid metals like sodium and mercury, commonly used in the laboratory, the kinematic viscosity ν is much smaller than the magnetic diffusivity λ (e. g., $\nu_{sodium}=0.6\times10^{-6}m^2/s$, $\lambda_{sodium}=0.1m^2/s$). This implies that the hydrodynamic Reynolds number is much larger than the magnetic Reynolds number Rm. For super-critical conditions with $Rm \geq 1$ we have $Re \sim 0(10^5\text{-}10^6)$. This means, the flow is fully turbulent. Compared to turbulent shear stresses the viscous shear stresses and so the viscous term $(1/Re)\cdot(\nabla^2 \upsilon)$ can be neglected. Nevertheless, using Reynolds' representation for turbulent flow the form of equation 2.1a is maintained for fully turbulent flow conditions, if the velocity is defined as a mean value and the Reynolds number is based on an assumed constant eddy viscosity ν_t (see, e. g., Hinze (1975)). Tilgner & Busse (2002) studied this modified problem numerically employing spectral methods for the spatial resolution and finite differences for the time integration.

Their procedure to achieve numerically supercritical finite amplitude steady states is as follows: For a specified Reynolds number Re and a prescribed solenoidal velocity field the body force field $\mathbf{f}$ in equation 2.1a is calculated for $\mathbf{B}=0$. A suitable velocity distribution υ_0 which fills the whole sphere and has a zero normal component at the surface is numerically constructed from the velocity field (see equation 2.4) by implementing a boundary adjustment function. This velocity field is taken as the initial kinematic state. As an initial magnetic state a small seed magnetic field

$$\mathbf{B} = \mathbf{B}_0 \tag{2.7}$$

is chosen according to possible laboratory conditions. As υ_0 acts already on the seed field $\mathbf{B}_0$, this effect is calculated from equation 2.1c to give a $\mathbf{B}_0$'. For a new set of Re and related R_m values a time integration of the equations 2.1 to a steady state is conducted starting from the initial velocity field υ_0 and the magnetic field $\mathbf{B}_0$'. The process can be continued to obtain for increasing values Re and Rm a set of growing finite amplitude values for the magnetic field at a particular location e.g. the centre of the sphere. In the terminology of bifurcation theory these non linear steady states represent the continuous branch of an imperfect pitch fork bifurcation (see Golubitzky & Schaeffer (1985)). The corresponding isolated branch can also be realized by numerical integration by changing at a high enough super critical Reynolds number the direction of the external magnetic field to the opposite direction , say to $\mathbf{B}_1$"=$\mathbf{B}_0$'–$\mathbf{B}_1$'. The time integration then leads to a steady magnetic field of opposite direction, if the intensity of the external magnetic field B'_1 has been properly chosen. If the external magnetic field is finally switched off and the integration is continued, steady solutions on the isolated branch are found in the same manner as obtained for the continuous branch. Figure 2.3 shows a typical bifurcation graph obtained by Tilgner & Busse (2002) for a parameter set compatible with the Karlsruhe Dynamo experiment. In their calculations they have normalised the magnetic field by the reference value $B_s = (\rho\mu)^{1/2}\lambda Rm/r_0$.

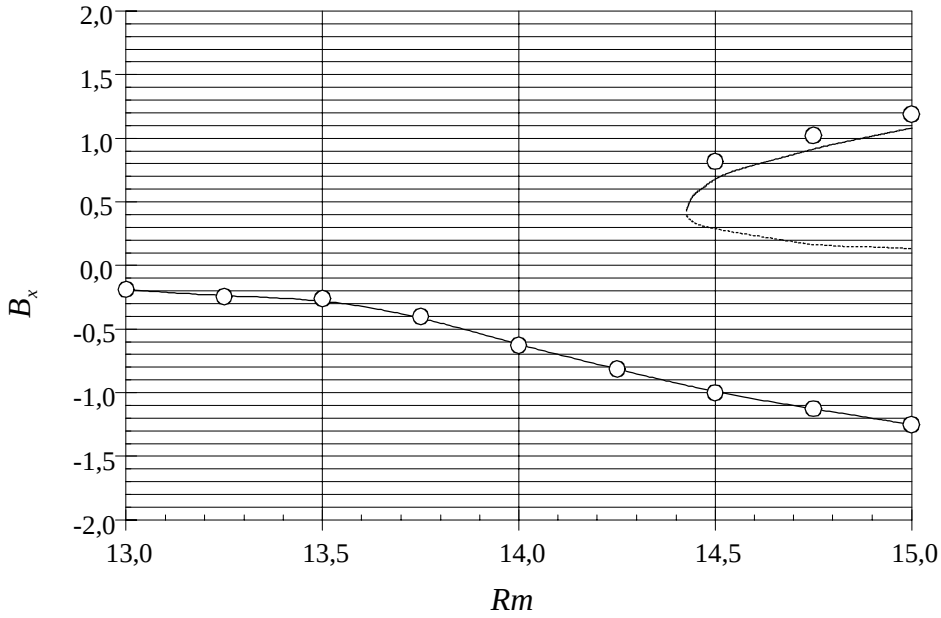

Figure 2.3: The bifurcation diagram for the Karlsruhe Dynamo experiment calculated by Tilgner & Busse (2002) for a dimensionless B_x and equal volumetric flow rates.

Tilgner & Busse (2002) have also proposed a model equation in a low order amplitude approximation for B . Their results are based on the general form of the equations 2.1 and suggest that the magnetic field saturates due to a reduction of the α- coefficient in the representation of the electromotive force by the "Mean Field Theory" with increasing field intensity. The reduction turns out to be proportional to $|\mathbf{B}|^2$. They derive an evolution equation for $\mathbf{B}$ in the form:

$$\frac{d\mathbf{B}}{dt} = \left[(\alpha - \beta |\mathbf{B}|^2) - \alpha_{crit}\right]\mathbf{B} + \mathbf{f}_B \tag{2.8}$$

where $\mathbf{f}_B$ accounts for the driving effect of an external seed field B_0 and α_{crit} is the value for the marginal state in case of a vanishing seed field.

By linking $\mathbf{f}_B$ to $\mathbf{B}_0$ and α_{crit} by $\mathbf{f}_B = \alpha_{crit}\,\mathbf{B}$ and setting $\alpha = c\,Rm$ they arrive at the following model equation for the amplitude B of the magnetic field.

$$|\mathbf{B}|^3 - (R_m - R_{m\,crit})\frac{c}{\beta}|\mathbf{B}| - R_{m\,crit}\frac{c}{\beta}|\mathbf{B}|_o = 0 \ . \tag{2.9}$$

This equation contains three independent coefficients Rm_{crit}, $|\mathbf{B}|_0$, c/β which may be adjusted to either numerical or experimental results. Rm_{crit} may be taken from calculations for the ideal kinematic state without seed field. $\mathbf{B}_0$ and c/β can be determined by fitting the third order equation to numerically or experimentally obtained solutions on the continuous branch. Then, the model equation predicts the discontinuous branch in the same approximation and the quality of the approximation can be tested by comparison with corresponding numerical and experimental results. The linear and non-linear behaviour of dynamo action in the Karlsruhe test facility has also been studied by Rädler et al. (2002a,b). Some of their results will be outlined in chapter 5.

2.4 The linear dynamics of magnetic fluctuations at mean stationary, supercritical states

This section is intended to substantiate observed fluctuations of the dynamo magnetic field as an interaction of Alfvén waves generated in each individual helical vortex of the velocity model in figure 2.2. Alfvén waves are excited, if lines of force are displaced by convective transport and magnetic stresses act to restore the displacement. A dynamo magnetic field with an orientation perpendicular to the mean flow in each helical vortex would be subjected to this effect. Based on this conception we recall a fundamental relationship for linear Alfvén waves. To facilitate our considerations we start, e.g. from a velocity field in the form of equation 2.4. We choose the amplitudes A and C such that the flow becomes a Beltrami flow. This is the case for C/(A$\sqrt{2}$). We shall next rederive formally a linear equation for Alfvén waves and the associated dispersion relationship.

The Mean Field Theory of turbulent flows applies a decomposition of the variables in a mean and a fluctuating part. We may therefore set

$$\mathbf{\upsilon}=\overline{\mathbf{\upsilon}}+\mathbf{\upsilon}',\ p=\overline{p}+p',\ \mathbf{B}=\overline{\mathbf{B}}+\mathbf{b}'.$$

For our special velocity distribution of equation 2.4 the large scale spatial average across the cylinder vanishes. The only relevant large scale quantity is the mean magnetic field. We assume that $|\overline{\mathbf{B}}| \gg \left|\overline{b'^2}\right|^{1/2}$ and that, as previously discussed, $Re \gg 1$. Then, we linearize the Lorentz force, neglect the viscous term in equation 2.1a and also linearize the convective term in the induction equation 2.1c. The two equations can then be written as

$$\partial_t\mathbf{\upsilon}'+\nabla\left(\frac{1}{2}\mathbf{\upsilon}'^2+\frac{p}{\rho}+\Phi\right)-\mathbf{\upsilon}'\times(\nabla\times\mathbf{\upsilon}')+(\nabla\times\overline{\mathbf{B}})\times\mathbf{b}'+(\nabla\times\mathbf{b}')\times\overline{\mathbf{B}}, \tag{2.10a}$$

$$\partial_t\mathbf{b}'=-\nabla\times(\overline{\mathbf{B}}\times\mathbf{\upsilon}')+\frac{1}{Rm}\nabla^2\mathbf{b}'. \tag{2.10b}$$

Here Φ is the potential of the forcing function $\mathbf{f}$ in equation 2.1a. We now consider $\overline{\mathbf{B}}$ to be the saturated supercritical state. For simplicity and with regard to theoretical results and experimental observations we set

$$\overline{\mathbf{B}}=(0,B_0,0),\ \mathrm{B_0} = \text{const.} \tag{2.11}$$

Furthermore, we rescale the dimensionless magnetic field $\mathbf{b}'$ to the new reference scale B_0. This is done by dividing the Lorentz force terms in equation 2.10a by the velocity ratio $A=U_o/V_a$, where V_a is the Alfvén velocity defined as $V_a = B_o(\mu\rho)^{-1/2}$ and U_0 the volumetric flux in a helical vortex of the velocity field equation 2.4. The velocity ratio A is denoted the Alfvén number. We follow Davidson (2001) and introduce the vorticity and current density, respectively, by

$$\mathbf{\omega}=\nabla\times\mathbf{\upsilon}',\qquad \mathbf{j}=\nabla\times\mathbf{b}'. \tag{2.12a,b}$$

Assuming that the velocity field υ' is a Beltrami flow, equation 2.10a reads as

$$\frac{\partial}{\partial t}\boldsymbol{\omega}=\frac{1}{A}\frac{\partial}{\partial y}\mathbf{j}. \tag{2.13}$$

Equation 2.10b takes the form

$$\frac{\partial}{\partial t}\mathbf{j}=\frac{\partial}{\partial y}\boldsymbol{\omega}+\frac{1}{R_m}\nabla^2\,\mathbf{j}. \tag{2.14}$$

Eliminating ω from equation 2.13 and 2.14 gives

$$\frac{\partial^2}{\partial t^2}\mathbf{j}-\frac{1}{A^2}\frac{\partial^2}{\partial y^2}\mathbf{j}-\frac{1}{R_m}\nabla^2\frac{\partial}{\partial t}\mathbf{j}=0\,.$$

This is a wave equation describing the propagation of Alfvén waves in y-direction. A solution can be readily given in the form

$$\mathbf{j} = \mathbf{j}_0\, exp\; i\,(k_y y - \Omega t) \tag{2.15}$$

for which the dispersion relation

$$\Omega=-\frac{1}{2}\frac{k^2}{Rm}i\pm\left[\frac{k_y^2}{A^2}-\frac{1}{4}\frac{\mathbf{k}^4}{Rm^2}\right]^{1/2} \tag{2.16}$$

holds. This relation describes a propagating Alfvén wave with an amplitude which is damped by Ohmic dissipation. There are two distinct asymptotic cases for very high and very small magnetic Reynolds numbers:

1 the oscillatory dampened Alfvén wave with propagation speed $1/A$ and $\Omega=-\mathbf{k}^2(2Rm)^{-1}\cdot i\pm(k_y/A)$;

2 the monotonically dampened wave with $\Omega = -\,\mathbf{k}^2/Rm\; i$. For intermediate values of $Rm \geq 1$ the frequency Ω and the propagation speed $c = \Omega/k$ depend on the wave vector k and the magnetic Reynolds number. Because of the difference expression in the radicant of equation 2.16 both quantities decrease for decreasing Rm compared to the case without Ohmic dissipation. We introduce the relevant physical scales according to equations 2.2 and 2.4 with the length scale a and the velocity scale U_0 and consider a wave of least damping which propagates in y-direction.

We obtain

$$2\pi f=-\frac{\pi^2}{2}\cdot\frac{\lambda}{a^2}i\pm\left[V_a^2\cdot\pi^2-\frac{1}{4}\frac{\pi^4}{a^4}\lambda^2\right]^{1/2}, \tag{2.17}$$

$$2\pi f=-\frac{\pi^2}{2}\frac{\lambda}{a^2}i\pm\frac{\pi^2}{2}\frac{\lambda}{a^2}\left[\frac{V_a^2}{V_D^2}-1\right]^{1/2}$$

where V_D is defined as the diffusion velocity $V_D = \lambda\cdot\pi/(2a)$. This result shows that at a saturated dynamo state magnetohydrodynamic waves can propagate and transfer energy. It is obvious that oscillatory wave propagation can only occur, if the Alfvén wave speed V_a is larger than the diffusion velocity V_D. Furthermore, the oscillation frequency decreases for $V_a \geq$

V_D, if V_a approaches V_D, i.e. if the intensity of the magnetic field decreases. Therefore, the frequency of the magnetic field fluctuations should increase with increasing intensities of the dynamo magnetic field. We shall see in section 4.5 that this conforms with some experimental observations.

2.5 Some comments on MHD-turbulence

In the Karlsruhe Dynamo experiment dynamo action occurs at high hydrodynamic Reynolds numbers $Re = \bar{u} \cdot d_H / \nu$ of the order 10^6 and magnetic Reynolds numbers $R_m = \bar{u} \cdot d_H / \eta$ of the order 1-10 (d_H is the relevant hydraulic diameter of a vortex generator, see figure 3.1 and the velocity $\bar{u}$ is the volumetric flux in it.). Thus, the channel flow is fully turbulent and all magnetohydrodynamic variables are affected by turbulent fluctuations. The quality of these turbulent fluctuations can be judged by utilizing the characteristic functions of random processes. In our analysis of measured time signals we shall evaluate the mean values, the probability density functions (PDF) and the higher moments, the variance, skewness and flatness (σ^2, S, K). The temporal and spatial coherence of the signals can be recognized from their auto- and cross-correlation functions. The definition of these function and more about their physical meaning for turbulent flows can be found in classical textbooks on turbulent flows (Tennekes & Lumley (1970), Hinze (1970)).

A key issue for MHD-turbulence is the distribution of energy between the kinetic energy of the velocity fluctuations and the energy of fluctuations of the magnetic field. A measure for this quantity is the variance σ or its square root, the RMS-value, denoted here as u^* or $\mathbf{b}^*$ for the velocity and magnetic field fluctuations respectively.

For a more subtle analysis of turbulent processes the exchange and transport of energy between the different size structures of the velocity and the magnetic field must be considered where the structures can be imagined as eddies of either the velocity or current field. The scale of these structures is limited by viscous and Joule dissipation on the lower side by the Kolmogorov (1941) time and length scales (see Hinze (1975)) . They read for the viscous and Joule dissipation as

$$\tau_{K\nu} = \left(\frac{\nu}{\varepsilon}\right)^{1/2}, \; L_{K\nu} = \left(\frac{\nu^3}{\varepsilon}\right)^{1/4} \quad \text{viscous dissipation,} \tag{2.18}$$

$$\tau_{K\lambda} = \left(\frac{\lambda}{\varepsilon}\right)^{1/2}, \; L_{K\lambda} = \left(\frac{\lambda^3}{\varepsilon}\right)^{1/4} \quad \text{Joule dissipation.}$$

Here ε is the specific energy flux which is dissipated. It may be defined by the large scale velocity u and its characteristic gradient

$$\varepsilon = u^3/l$$

or in case of channel flow by the pressure loss Δp, the volumetric flow rate $\dot{V}$ and the fluid mass M as

$$\varepsilon = \dot{V} \cdot \Delta p / M \; .$$

The upper limit of scales is determined by the dimensions of the test facility. This is in our case typically for the velocity $\bar{u}$ the diameter d_H of a vortex generator, for the magnetic field and the associated currents the diameter of the cylindrical test module $2r_0$. An appropriate time scale for the magnetic field has to be based on the Alfvén velocity defined by an external magnetic field or, in case of dynamo action, on the induced magnetic field.

The energy transfer between the different scales is commonly discussed in turbulence theory by a spectral decomposition of the state variables and a spectral transformation of the governing equations, in our case equations 2.1. The variables in the so-called Fourier space depend on wave numbers k_n and frequencies ω_n which are related to the corresponding length and time scales of the turbulent structures as

$$k_n = \frac{2\pi}{L_n},$$

$$\omega_n = \frac{2\pi}{\tau_n}.$$

For turbulent channel flow, where $u^*/\bar{u} \ll 1$ holds, Taylor's hypothesis (see Hinze (1975)) applies and k_n can be expressed by ω_n and the mean velocity as $k_n = \omega_n / \bar{u}$.

With this in mind we carry on with the further discussions on turbulent energy transfer in the wave number space. The spectral distribution of the turbulent energies is obtained by a Fourier transformation of the auto-correlation function of the velocity and magnetic field fluctuations respectively. One obtains the turbulent energies E^V and E^M defined as

$$E^V = \int_0^\infty E_k^V(k)\,dk\,,\; E^M = \int_0^\infty E_k^M(k)\,dk \quad ^{1)},$$

where E_k^V and E_k^M are the energy distributions of the velocity and the magnetic field. In three-dimensional turbulent flow, not influenced by strong magnetic fields or intensive rotation, the kinetic energy of large scale motion is transferred to smaller scale motions in a cascade of successive flow instabilities induced by vortex stretching and shearing processes. This occurs without dissipative losses in a wave number range between the low wave number k_L of the large scale inertial flow and the high wave number $k_{K\nu}$ for viscous dissipative small scale flow. Based on the assumption that the flux of kinetic energy is conserved, a relation between the spectral energy density E_k^V, the injected energy rate ε and the wave number k can be derived in the form

$$E_k^V = c_K \varepsilon^{2/3} k^{-5/3} \qquad \text{in} \quad k_L < k < k_{K\nu} \tag{2.19}$$

with $k_{K\nu}$ as the wave number based on the Kolmogorov viscous dissipative length scale (Kolmogorov (1941), Tennekes & Lumley (1977)). This is called the inertial range of kinetic energy transfer by a non-linear interaction of vortices and for negligible viscous dissipation. The transfer process has to be modified in conducting fluids in the presence of a magnetic field, as the small scale motions are influenced by large scale magnetic fields. This may be

[1] The formalism of spectral decomposition holds strictly only for homogeneous turbulent flows in infinite domains (see textbooks on turbulent flows).

an external magnetic field or a self-exited mean magnetic field $\overline{B}$. The energy transfer may occur through Alfvén waves in an inertial range of wave numbers which is limited from above by the Joule dissipative wave number $k_{K\lambda} = 2\pi\left(\varepsilon / \lambda^3\right)^{1/4}$. Irishnikov (1964) and Kraichnan (1965) derived an interdependence between the spectral energy E_k^V, the dissipation ε and the Alfvén velocity V_a (see section 2.4). They used dimensional arguments based on the assumption that the energy flux was constant and an equipartition of kinetic and magnetic energy holds in the inertial wave number range. They arrive at the following power relationship for the kinetic spectral energy:

$$E_k^V\ (k) = c_K(\varepsilon V_a)^{1/2}\, k^{-3/2} \quad \text{in } k_L < k < k_{K\lambda}. \tag{2.20}$$

This relationship holds as long as the velocity and magnetic field fluctuations are spatially uncorrelated, which is true for low intensity mean magnetic fields and the interaction of waves with the same size wave numbers. However, if the velocity and magnetic field become correlated at increasing magnetic field intensities, the energy exchange by Alfvén wave interaction occurs in a wide range of wave numbers. Equipartion between kinetic and magnetic energy can not be anticipated anymore. This case has been treated by Grapin et al. (1983)[2]. Using Elsasser variables $\mathbf{Z}^{\pm} = \mathbf{\upsilon} \pm \mathbf{B}/(\rho\mu)^{1/2}$ they consider modified spectral quantities based on these variables and relate them to the energy spectral densities $E_K^v(k)$ and $E_k^M(k)$. They define

$$E_k^{\pm} = \frac{1}{4}\int \left|\mathbf{Z}_K^{\pm}\right|^2 d\Omega_K\,, \quad E_k^R = \frac{1}{2}\int \mathbf{Z}_K^{+}\,\mathbf{Z}_K^{-}\, d\Omega_K\,,$$

where Ω_K is the angle in the k-space. By definition the following relations hold between the total spectral energy E_K and the Elsasser spectral energy quantities $E_k^{\pm}$

$$E_k = E_k^V + E_k^M = E_k^+ + E_k^- \quad ,$$

$$E_k^R = E_k^V - E_k^M\ .$$

Making assumptions of strong separation of scales in the inertial range, i.e., $k \ll k_+$, but requiring equal dissipation wave numbers $k_{K\lambda}$ for both Elsasser spectral energy densities, Grapin et al. (1983) derive the following power laws for the inertial range

$$E_k^{\pm} \approx C_1 \lambda V_a \left(\frac{k}{k_{K\lambda}}\right)^{-m_{\pm}}, \tag{2.21}$$

with $m_+ + m_- = 3$ and

$$E_k^R = E_k^V - E_k^M = C_2 (V_a \cdot k)^{-2}. \tag{2.22}$$

These correlations merge into the Irishnikov-Kraichnan (1964, 1965) relationship under the assumption of equipartition between kinetic and magnetic spectral energies.

[2] See also Biskamp (1993)

The relations 2.21, 2.22 suggest that the decrease of the spectral energies E_K^V and E_K^M may be stronger in the inertial range in case of non equipartition of spectral energies and strong correlations between the velocity and the magnetic field fluctuations than predicted by the Irishnikov-Kraichnan relation 2.20. Indeed, Léorat et al. (1981) have performed numerical calculations on fully developed MHD- turbulence near critical magnetic Reynolds numbers using a spectral simulation of the MHD-equations 2.1 and turbulence models within the scope of the Eddy-Damped Quasi Normal Markovian (EDQNM) approximation. They find for supercritical magnetic Reynolds numbers power laws for the kinetic energy spectrum of the kind $E_k^V \approx k^{-2.4}$ and for the magnetic energy spectrum $E_k^M \approx k^{-4.4}$ which they attribute to an inertial range of the MHD-power spectra.

The spectral behaviour of the MHD energies under the influence of Joule dissipation but still in the inertial range of fluid dynamic wave numbers has been analysed by Moffat (1961). Assuming that $1 \ll Rm \ll Re$ holds, he finds that the magnetic spectral energy distribution is correlated to the kinetic spectral energy as

$$E_k^M \approx \lambda^{-2}\, k^{-2}\, E_k^V \,. \tag{2.23}$$

Using further for the kinetic spectral energy E_k^V of the Kolmogorov spectrum of equation 2.19 he proposes the following expression for the magnetic spectral energy in the Joule dissipative regime of wave number $k_{K\lambda} < k < k_{K\nu}$:

$$E_k^M = \frac{9}{4} Rm \cdot \overline{H}_o^2\, \varepsilon^{2/3}\, \lambda^{-2}\, k^{-11/3} \quad \text{in } k_{K\lambda} < k < k_{K\nu} \,. \tag{2.24}$$

Here $\overline{H}_o^2$ is the magnetic energy of the large scale magnetic field, e.g., an external magnetic field or a self-exited dynamo field. Compared to the spectral energy behaviour in the inertial range with assumed equipartion of energies, this relationship indicates a strong reduction of the turbulent magnetic energy with increasing wave numbers, as Joule dissipation destroys the eddy currents and thus the small magnetic field variations.

If large scale magnetic fields have an intensity such that Lorentz forces become significant for the momentum transfer, even local homogeneity of the velocity field can not be sustained. Velocity fluctuations in the direction of the magnetic field and perpendicular to it are differently dampened by Joule dissipation and there is a quasi-equilibrium transfer of energy between the fluctuations of different spatial orientation. The effect has been analysed in detail by Alemany et al. (1979). The effect should be observed if the interaction parameter based on the local quantities, the *RMS* value of the velocity fluctuation u^*, the vortex dimension ℓ and the magnetic field intensity B_0 is of the order *one,* i. e.

$$N = \frac{\sigma B_o^2\, \ell}{\rho\, u^*} \approx O(1)$$

(With regard to the model velocity field in figure 2.2 and dynamo action, B_0 would correspond to the self-excited magnetic field intensity $|\mathbf{B}|$ and u^* to the mean helical velocity $\bar{u}$ defined as the helical volumetric flux; ℓ would correspond to the half period *a* of the velocity field.)

Equivalently it can be stated that the transport time of energy or the vortex turn over time $\tau_t \sim \ell / u^*$ is of the same order as the Joule dissipation time scale $\tau_j \sim \rho/(\sigma B_0^2)$.

With $\ell \sim 1/k$ and a spectral representation of the velocity , $u^* \sim (E_k^{(v)} k)^{1/2}$, this results in the power relationship:

$$E_k^V \sim \tau_j^{-2} k^{-3}. \tag{2.25}$$

If the condition $N \sim O(1)$ holds and, as a consequence, for the spectral kinetic energy the power law (2.25) is valid, then the spectral behaviour of the magnetic energy will be modified in the wave number range larger than the wave number k_{in} at which energy or helicity is injected into system. In a subrange $k_{in} < k < k_{K\lambda}$ we may assume an equipartition of spectral kinetic and magnetic fluctuation energies, as we may neglect magnetic diffusion effects in the transport equation of the magnetic field and, furthermore, linearise in the fluctuation terms. This gives for the spectral magnetic energy distribution [3]

$$E_k^M \sim E_k^V \sim \tau_j^{-2} k^{-3}. \tag{2.26}$$

For the Kolmogorov wave number range $k_{Kv} > k > k_{K\lambda}$ of diffusive magnetic losses insert the spectral kinetic energy distribution (2.25) applies. This inserted it into relationship (2.23) for the spectral magnetic energy gives

$$E_k^M \approx \lambda^{-2} \tau_j^2 k^{-5}, \text{ for } k > k_{K\lambda}. \tag{2.27}$$

This power law indicates a very rapid decrease of the magnetic spectral energy in the Kolmogorow range of wave numbers.

So far we have considered the spectral energy transport from large scale vortices and eddy currents downward to smaller scales. It has been observed, however, in model calculations that in three-dimensional turbulent vortical flow small scale magnetic energy associated with small scale eddy currents may build up large scale magnetic fields by self-organisation. This effect is known as reverse cascade of spectral energy transfer. This process has been described theoretically for helical turbulence in a series of papers by Frisch et al. (1975), Pouquet et al (1976), Leorat et al. (1981). Here we outline some results of Pouquet et al. relevant for the discussion of our observations.

In magnetohydrodynamics the magnetic helicity is a conserved quantity, if dissipative effects are neglected. It is defined as

$$H = \frac{1}{V} \int_V \mathbf{A} \cdot \mathbf{B} \, dV \quad \text{with} \quad \mathbf{B} = \nabla \times \mathbf{A}, \; \nabla \cdot \mathbf{A} = 0,$$

---

[3] The proportionality between E_k^M and E_k^V can be derived from the transport equation for the magnetic field for vanishing diffusivity λ. For this case $\dot{\mathbf{B}} = \nabla \times (\upsilon \times \mathbf{B})$. Decomposing $\mathbf{B}$ as usual in $\mathbf{B} = \overline{\mathbf{B}} + \mathbf{b}'$ and $\upsilon = \mathbf{U} + \mathbf{u}'$ and Fourier-transforming the equations one obtains

$$\omega_k b_n = \overline{B} \, k_n \, u_n .$$

Using the relationship $b_n = (E_n^M k_n)^{1/2}$, $u_n = (E_n^V k_n)^{1/2}$ and $\omega_n / k_n = \overline{U}$

we get $E_n^M = \overline{B}^2 / (\overline{U}^2) E_n^V$

where $\overline{U}^2$ is a measure for the injected kinetic energy and $\overline{B}^2$ represents the energy of the large scale magnetic field.

and it is

$$dH/dt = 0 \quad \text{for } (\lambda,\nu) \rightarrow 0.$$

Here **A** is the magnetic potential. Frisch et al. (1975) pointed out that in the spectral domain of helical, isotropic MHD-turbulence a self-organisation of this quantity towards larger scales may occur. This reverse cascade has been corroborated by Pouquet et al. (1976) by extensive numerical calculations using the EDQNM-approximation for turbulent helical flow in the spectral domain. They find that together with the reverse helicity cascade a reverse energy cascade exists. Their time integrations in the spectral domain suggest that energy transfer to smaller wave numbers approaches an equilibrium steady state, if energy or magnetic helicity is injected into the turbulent system at a fixed rate and a characteristic scale, say, wave number k_{in}. In the spectral domain their results indicate a quasi-stationary behaviour in form of power relationships

$$H_k^M(k) \sim k^{-2}, \quad E_k^M(k) \sim k^{-1}; \tag{2.28}$$

for the magnetic spectral helicity H_k^M and the magnetic spectral energy E_k^M. They support these findings by dimensional arguments of the Kolmogorov type for the reverse inertial transport mechanisms. They argue that there should exist a unique functional dependence between the relevant quantities E_K^M and $H_K(k)$ on the one side and the effective helicity injection rate ε_{eff}^M and the wave number k on the other side. The effective helicity injection rate may differ from the total injection rate, as a part of it may cascade into helicities of smaller scale and finally dissipate. A similar statement holds for the injected energy. The dimensional considerations result in the relationships

$$E_k^M(k) = C_1(\varepsilon_{eff}^M)^{2/3} k^{-1}, \; H_k^M(k) = C_2(\varepsilon_{eff}^M)^{2/3} k^{-2} \quad \text{for } k < k_{in}, \tag{2.29a,b}$$

where C_1 and C_2 are dimensionless constants.

From an experimental point of view for dynamo action the injected kinetic helicity is the actual control parameter rather than the magnetic helicity.

Under the random action of small scale Alfvén waves it may be assumed that the kinetic and magnetic energies and helicities relax to quasi-equipartition. Using the conservation equations for these quantities in the spectral domain (Pouquet et al. (1976)) the following relationship

$$H_k^V \approx k^2 H_k^M, \tag{2.30}$$

can be obtained. Here H_K^V is the spectral representation of the kinematic helicity

$$H^V = \frac{1}{V}\int_V \mathfrak{v} \cdot (\nabla \times \mathfrak{v}) dV. \tag{2.31}$$

This relationship holds also for the effective injection rate of this quantity i. e. $\varepsilon_{eff}^M \approx k^{-2}\varepsilon_{eff}^V$.

Following Pouquet et al. (1976) we give an estimation for the time it takes to build up a large scale magnetic field of dimension $L \sim k_L^{-1}$ from a small scale turbulent seed field char-

acterized by an injection length scale $\ell_{in} \sim k_{\ell}^{-1}$. It is reasonable to define this time to be proportional to the ratio

$$T \sim \frac{H^M}{\varepsilon_{eff}^M}. \tag{2.32}$$

This is the magnetic helicity contained in the large scales divided by its effective injection rate. An integration of equation 2.29b gives:

$$H^M = \int_{k_L}^{k_{in}} H_k^M \, dk = C_2 \, (\varepsilon_{eff}^M)^{2/3} \, (L - \ell_{in}).$$

Furthermore we get

$$T \sim (\varepsilon_{eff}^M)^{-1/3} \, (L - \ell_{in}).$$

Using relationship 2.30 results in

$$T \sim C_2 \, (\varepsilon_{eff}^V \cdot \ell_{in}^2)^{-1/3} \, (L - \ell_{in}). \tag{2.33}$$

We shall utilize the outlined relationships for turbulent MHD-flow in our discussions of the experimental results in chapter 5.

3 The dynamo test facility and instrumentation

The Karlsruhe dynamo test facility has been described in detail by Stieglitz & Müller (1996). Here we restrict ourselves to a brief outline of the main features. The test rig consists essentially of a cylindrical dynamo module which contains 52 vortex generators connected to three different loops each of which is equipped with a magnetohydrodynamic feed pump of about 210 kW power and heat exchanger to assure constant temperature in the liquid sodium during the experimental runs. Using a water-steam heat exchanger allows to keep the operation temperature within a threshold of $\pm 1°K$ during runs of several hours. The module and the loop are entirely fabricated of stainless steel. The outer hull of vortex generators as well as the inner tube consist of 1 mm thick stainless steel sheets or tubing material, whereas the guide vanes producing the vortical flow are built up of 0.5 mm thick material. Taking into account the different specific electric conductivites of stainless steel and sodium and operating the dynamo module in a temperature range between $120°<T<125°C$ yields a magnetic diffusivity of $\lambda=0.1 m^2/s$ with an accuracy of $\pm 0.002\ m^2/s$.

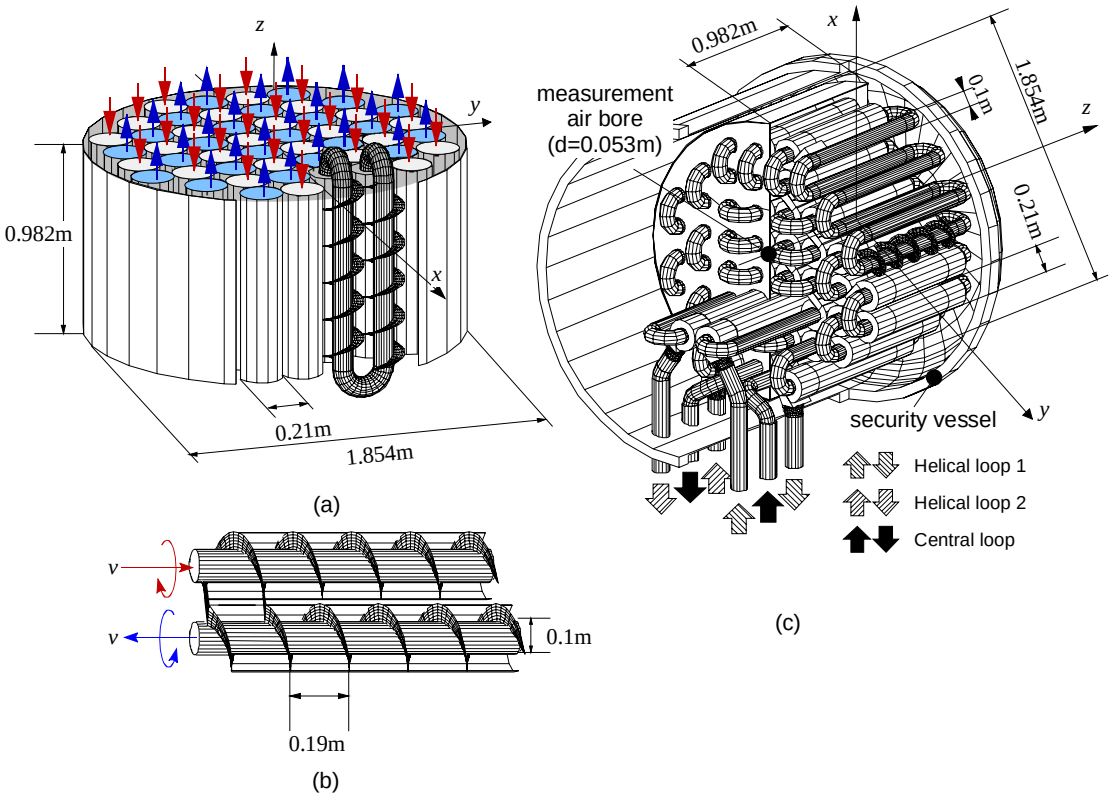

Figure 3.1: Semi-technical sketch of the Karlsruhe dynamo test module. a) internal structure and velocity distribution; b) vortex generator; c) technical design.

A semi-technical sketch of the dynamo module, the individual vortex generator and the operational set up is seen in figure 3.1.The ideal helical flow of the vortex pattern according to equation 2.4 is approximated by a quasi vortex free flow in the central duct and a spiral flow in the annular gap enforced by a helical baffle plate. The diameter of a vortex generator is

$a=0.21m$; the inner duct diameter is $a_i=0.1m$. The height of a complete helical winding is $h=0.19m$. The radius of the cylindrical container is $r_0=0.85m$, its height is $d=0.9m$. The vortex generators are interconnected at their ends by bends for the central flow and by fitting channels for the helical flow. The helical flow in the vortex-generators is provided by two separate loops each supplying 26 helical flow channels arranged in a right and left semi-section of the cylinder. The central flow is controlled by a third sodium loop. The maximum capacity of the MHD-pumps is $\dot{V}=150m^3/h$ each. The pressure drop across the module in each of the three independent channel systems is measured by sensitive capacitance pressure gauges with an accuracy of $\delta p=\pm 5\cdot 10^2 Pa$. The sodium volumetric flow rate in each of the three loops is determined by electromagnetic (EM) flow meters which are calibrated to give errors less than $(\delta\dot{V})/\dot{V}\leq 3\%$.

The module is located in a separate room and sheltered against electromagnetic stray fields from the MHD-pumps and EM-flow meters by soft iron plates. Thus, the intensity of the stray field in the test room is less than $0.5\ Gauss\ (G)$, i.e. of the order of the Earth's magnetic field. The magnetic field in the test module is measured by Hall sensors with a resolution of $\delta B\leq 0.05G$. During the dynamo tests the magnetic field is recorded at two fixed locations near the equator of the cylinder, separated at 120°, and on variable positions along the cylinder axis between the center and the "North Pole" using a traversible probe. Two Hall sensors ($H3$,$H4$) are fixed to the traversible probe. One ($H3$) is capable to measure all three components (B_x, B_y, B_z) of the B-field, the other ($H4$) located at a distance of $135\ mm$ from the first one measures B_y only. The Hall sensors near the equator ($H5$,$H6$) are arranged to measure the radial component of the field. One of them ($H5$) also measures the axial component B_z. The sensor locations are schematically shown in figure 3.2.

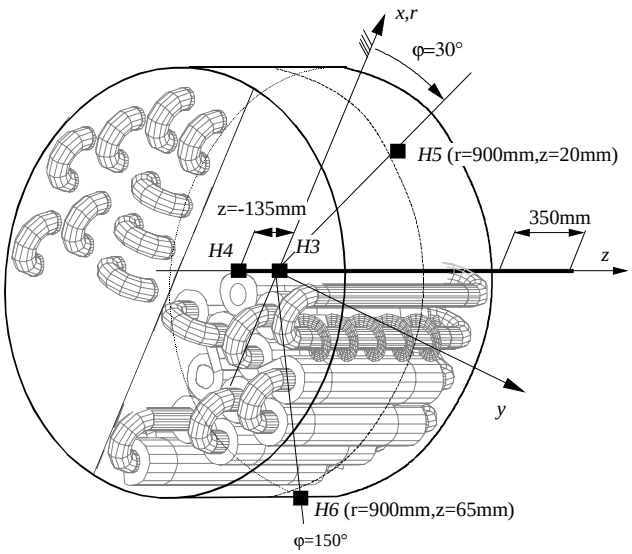

Figure 3.2: Sketch of the locations of the Hall sensors in the test module at location $H3$: two Hall sensors to measure three field components B_x, B_y, B_z; location $H4$: one Hall sensor to measure B_y; location $H5$: one Hall sensor to measure two components B_z and B_r, i.e. the radial component; location $H6$: one Hall sensor to measure the radial component B_r.

Before each measuring campaign of a day the pressure-transducers, the EM-flowmeters and the Hall sensors were calibrated to assure high measuring accuracy and to avoid systematic errors. In particular the flow rate was calibrated before each coherent set of measurements. Also the environmental seed magnetic field was repeatedly recorded with the traversable Hall sensors for vanishing volumetric flow rates and at intermediate subcritical flow rates. Two typical recordings for the mean magnetic field intensities on the module axis in the range $0\ mm \le z \le 350\ mm$ are shown in the graphs of figure 3.3a, b for flow rates indicated in the figure captions. The graph shows that the seed magnetic field is subject to variations during a measuring period. However, the observed variations were always smaller than the local intensity of the Earth's magnetic field.

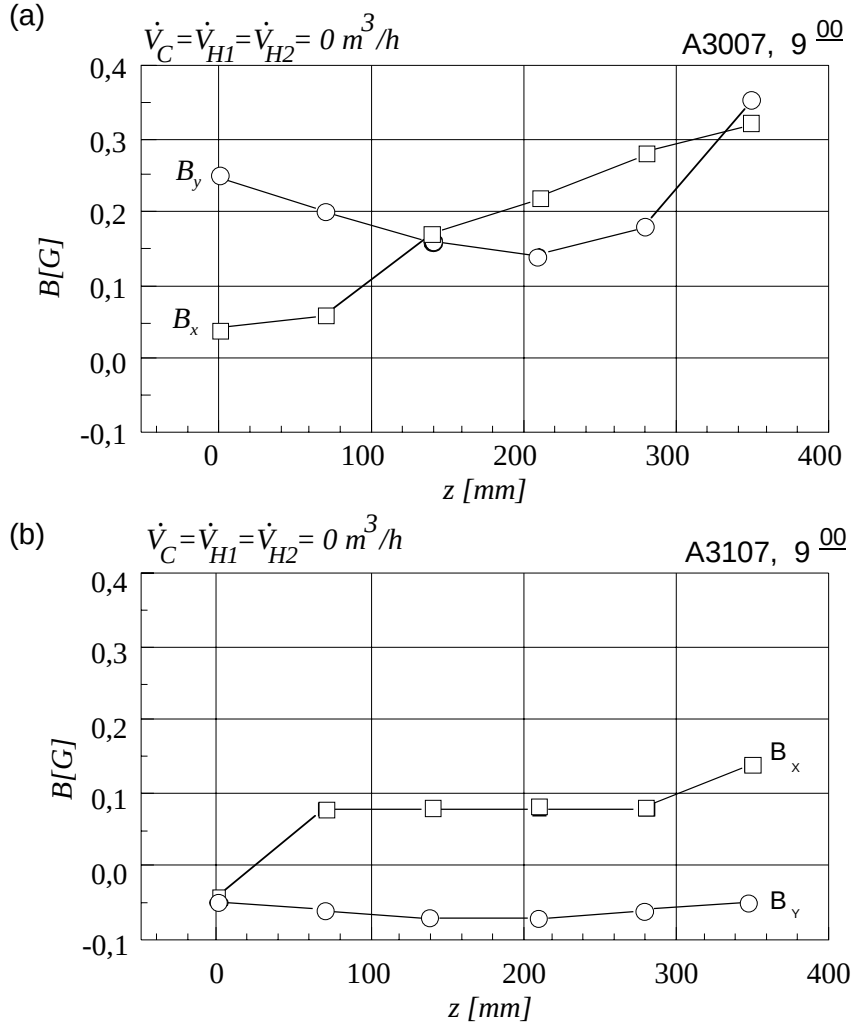

Figure 3.3: The distribution of the seed magnetic field along the module axis in the range $0 \le z(mm) \le 350$ recorded at (a) the beginning and (b) the end of a measuring campaign. There is a noticeable change in the local characteristic of the seed field. Volumetric flow rates $\dot{V}_C = \dot{V}_{H1,2} = 0\ m^3/h$; $\lambda = 0.1 m^2/s$.

Furthermore, arrays of mobile compass needles were attached to two vertical wood boards, one placed sidewise and one in front of the cylindrical dynamo vessel, in order to get a qualitative impression of the structure of the generated magnetic field. By the orientation of the compass needles during dynamo action the global structure of the magnetic field could be identified. In support to this qualitative instrumentation the normal component of the magnetic field with regard to the vertical boards was measured using a carry-on Hall probe in some cases.

The test module was operated generally in two modes. In order to study the onset of self-excitation and the saturation of the magnetic field at super-critical conditions, the volumetric flow rates in the three loops were scanned up (or down) in flow rate variations $0.1 \leq \Delta\dot{V}\ (m^3/h) \leq 5$ within time intervals of typically between 1 and 10 minutes to assure a new hydromagnetic equilibrium, i. e. a saturated dynamo state. The variation of one flow rate was performed, while the other helical or central flow rates were kept constant or all flow rates were simultaneously varied at the same rate.

The other operation mode of the test facility is concerned with long term runs at constant volumetric flow rates. Time series of signals of the magnetic field intensities, pressure differences, and volumetric flow rates were recorded during time intervals of 1200 up to 4000 seconds (s).

4 Results

4.1 Self-excitation of the magnetic field

In our experiments we used time series signals recorded by Hall probes, EM-flow meters and pressure-transducers respectively as indicators of dynamo action. Typical time signal recordings for the volumetric flow rates in the three loops, the three components of the magnetic field at the centre of the module (position *H3* in figure 3.2) and the pressure drop in the three channel systems of the module are shown in figure 4.1. In this experiment the two helical flow rates V_{H1} and V_{H2} were simultaneously raised stepwise from subcritical to supercritical conditions during a period of totally *1600* seconds, while the central flow rate was kept constant at $\dot{V}_C = 85 m^3/s$ or $86 m^3/h$.

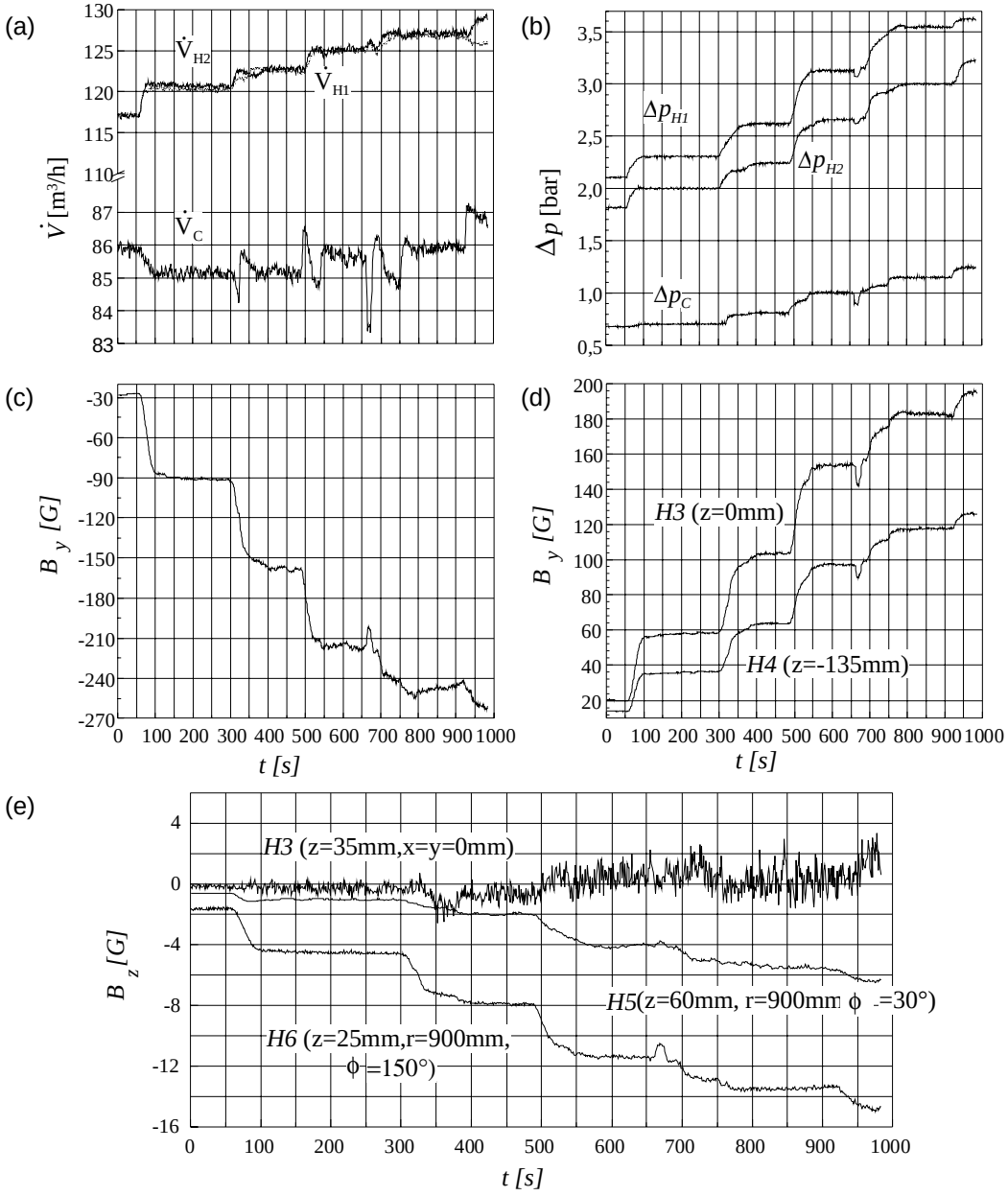

Figure 4.1 Time signal recordings for a) volumetric flow rates; b) pressure losses in the helical and central channels; c-d) magnetic field components for an experimental operation with stepwise changing flow rates.

The signals of the first 1000 seconds are displayed. The magnetic field components follow the stepwise variation of the helical flow rates and achieve a saturation level during each time interval without flow rate variation. There is particularly no delay time between the rise time of the volumetric flow rate and the one of the magnetic field components. An evaluation of the predicted self-organisation time for the large scale magnetic field according to equation 2.33 gives time scales of less than $0.6s$ which are much smaller than any realised rise time for the pumping power. After 900 seconds of test time the record shows a saturated B-field of $|B| \sim 300G$ in the centre of the module with strong x- and y-components and a small z-component.

In figure 4.2 the stationary states are plotted versus the helical flow rates. This graph shows a weak increase for lower and a strong increase for higher flow rates with a tendency to reduced growth rates at even higher flow rates. A point of inflection can be recognized in the interpolation curve of the measured data points. The onset of dynamo action can not be sharply allocated to a particular volumetric flow rate $\dot{V}_H$. The observation suggests a smooth rather than a sharp bifurcation i.e. imperfect bifurcation of the steady dynamo states from the hydrodynamic basic state. To quantify the near critical dynamo conditions it may be suggestive to draw the tangent to the interpolation curve of figure 4.2 in the inflection point and take its intersection with the flow rate axis as an indicator for onset of dynamo action. From a theoretical point of view this procedure underestimates the onset of dynamo action for the ideal case of an infinitesimal small seed magnetic field. In the laboratory there is at least the finite Earth's magnetic field which is first intensified by hydrodynamic stretching before real self-amplification occurs.

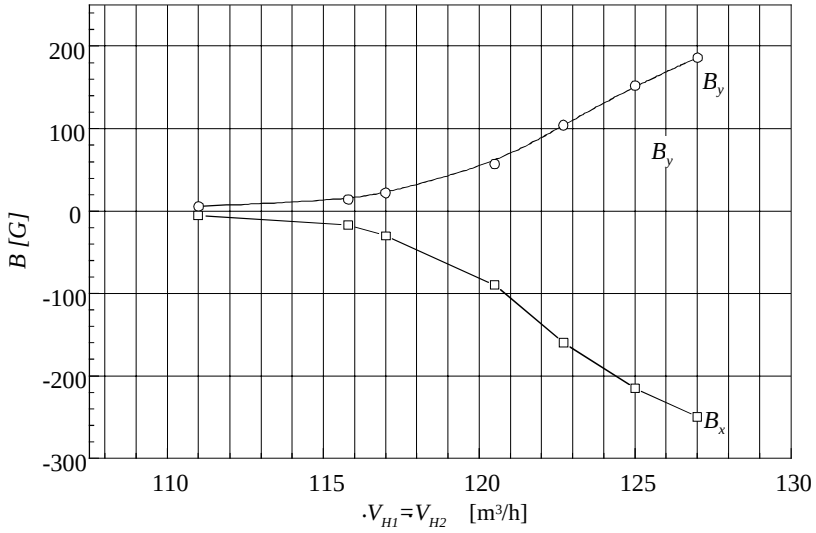

Figure 4.2: Magnetic field components B_x and B_y for saturated steady dynamostates for a constant central flow rate $\dot{V}_C = 85m^3/h$ and variable helical flow rates $110 < \dot{V}_{H1,2}\,(m^3/h) < 130$.

In a similar way as in case of hydrodynamic bifurcation problems of shear flow, the piping pressure loss across the module indicates the onset of self-excitation by a significant pressure increase due to the additional magnetohydrodynamic losses. In figure 4.3 the pressure differences between inlet and outlet of the three loops at the test module are shown for the corresponding steady hydrodynamic and magnetohydrodynamic states. The hydrodynamic

and magnetohydrodynamic flow states can be distinguished by a change in the increment of the data sequence. Linear interpolation curves for the hydrodynamic and the magnetohydrodynamic losses then define experimentally in a good approximation the bifurcation point for this particular test run. Here, we emphasise that the pressure loss measurements in the three independent loops result in the same transition value within a margin of $\Delta\dot{V}_H \leq 1\ m^3/h$ or a relative error of *1%*. Corresponding test runs were performed and evaluated for other fixed central and variable helical flow rates or in some cases vice versa, e. g., for a fixed flow rate $\dot{V}_C = 105\ m^3/s$ (see figure 4.3b).

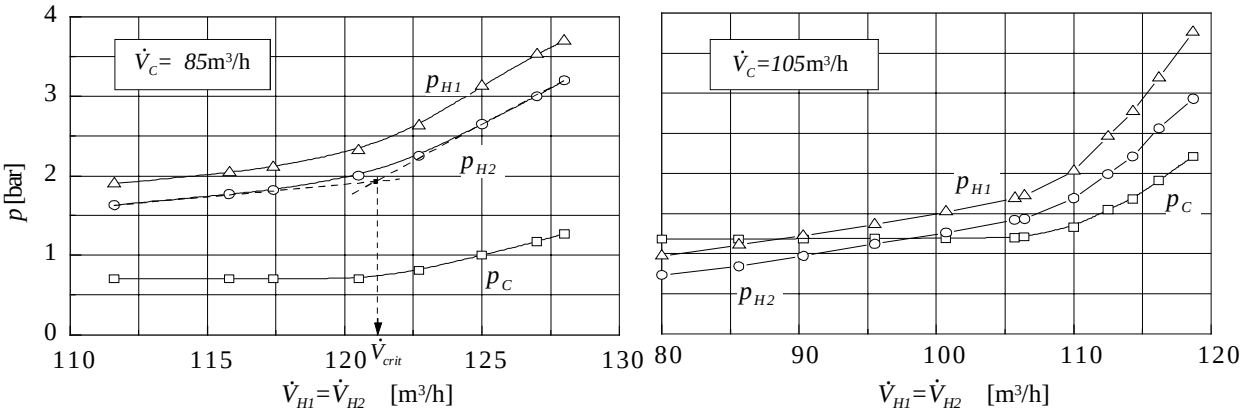

Figure 4.3: Pressure losses in the helical and central piping systems of the test module under steady state operation conditions for a) $\dot{V}_C = 85\ m^3/h$, $110 < \dot{V}_{H1,2}\,(m^3/h) < 130$; b) $\dot{V}_C = 105\ m^3/h$, $80 < \dot{V}_{H1,2}\,(m^3/h) < 120$.

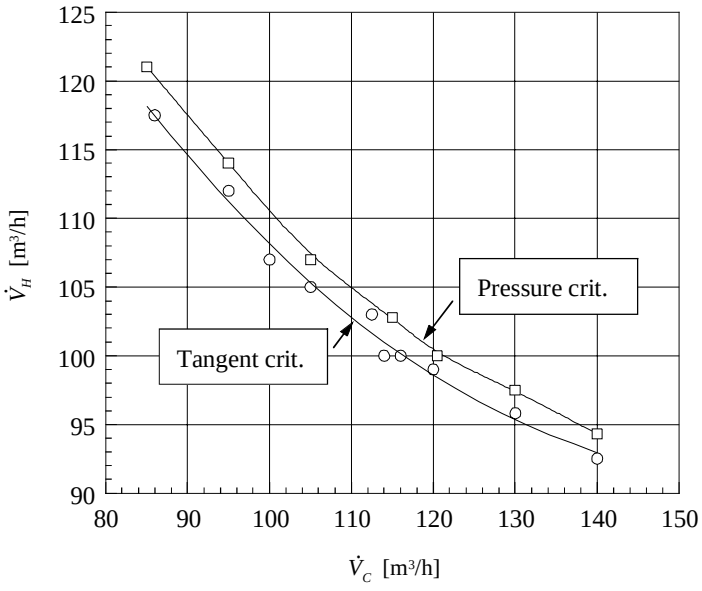

Figure 4.4: The state diagram for dynamo action for the Karlsruhe test module, □ pressure loss criterium; ○ tangent criterium.

The evaluation of the pressure losses results in a phase diagram of dynamo action for our test module presented in a $(\dot{V}_H, \dot{V}_C)$- plane in which hydrodynamic and dynamo states are separated by an interpolation line of hyperbolic character. This is seen in figure 4.4. The

state transition criterion extracted from this data set using the "tangent-inflection point" criterion, outlined above, is also plotted in figure 4.4 by a line. This line runs parallel to the pressure criterion curve but is shifted by about $\Delta\dot{V}_H \cong 2.5 m^3/h$ to the hydrodynamic side. The measured y-components of all observed steady magnetic fields are displayed in figure 4.5 as an interpolated isoline graph. The slight roughness of the isoline surface reflects the limited number of experimental data points and insufficient smoothing of the graphic software.

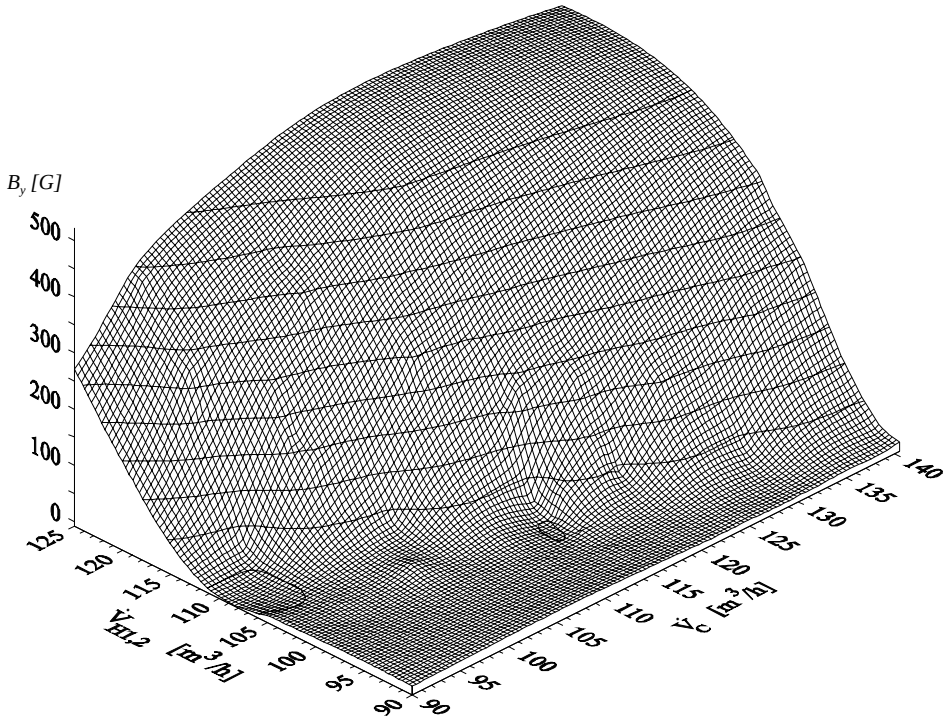

Figure 4.5: Isoline surface of the *y*-components of the magnetic field measured in the centre of the module depending on the helical and central volumetric flow rates $\dot{V}_C$ and $\dot{V}_{H1,2}$.

4.2 The structure of the magnetic field

The overall structure of the dynamo fields at clearly supercritical conditions was tested by the orientation of an array of compass needles arranged on plane boards which were placed vertically sidewise and in front of the cylindrical test vessel. The needles may turn in the plane of the board and thus react to the magnetic field components in this plane. A photograph of the needle array is shown in figures 4.6a,b. The particular test was performed for the volumetric flow rates $\dot{V}_c = \dot{V}_{H1} = \dot{V}_{H2} = 115 m^3/h$. The photo in figure 4.6a shows a set of needles of random orientation near the plate centre. Otherwise the orientation of the needles is towards the periphery of the plate. This indicates a source (or sink) of magnetic field lines near a centreline perpendicular to the cylinder axis of the module and suggests a dipole structure of the field. This impression is supported by photo 4.6b showing the orientation of compass needles at the front side of the module. Two centres of random needle orientation are located at a certain distance from the two vertical rims of the plate and slightly below (left side) and above (right side) its horizontal centreline.

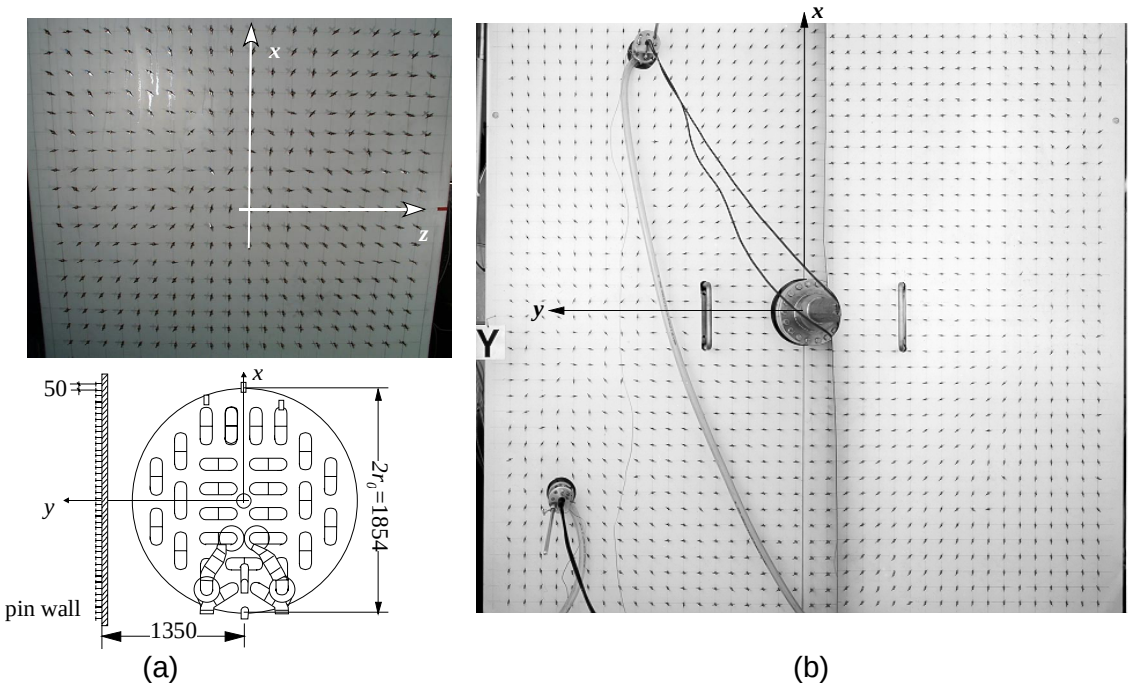

Figure 4.6 a.) Array of compass needles arranged on vertical wood boards sidewise of the test module and parallel to its axis; b.) in front of the module and perpendicular to its axis. Experimental conditions: $\dot{V}_C = 134 m^3/h$, $\dot{V}_{H1,2} = 101 m^3/h$ and $\lambda = 0.1 m^2/s$.

Between these centres and towards the plate periphery the needles show an orientation along lines of force which are compatible with a quasi-dipole field whose axis penetrate the module perpendicular to the cylinder axis and is slightly tilted. This observation is supported by an isoline field of the normal components of the magnetic field, which were measured by a carry-on Gauss meter on the sidewise located board. The isoline plot is shown in figure 4.7. The centre of largest field intensity coincides nearly with the area of disorder in the needle array at the side board (see figure 4.8b).

Further insight into the local structure of the magnetic field is gained by the distribution of the field components along the cylinder axis obtained by traversing the Hall probe in the range $0 \le z \le 350mm$. This distribution is shown in figure 4.8a for the volumetric flow rate condition $\dot{V}_c = \dot{V}_{H1} = V_{H2} = 115 m^3/h$. There is only a small B_z-component compared to the B_x and B_y components. The maximum of the field intensity is not achieved in the centre of the module. There is rather a small shift of the maximum towards a position $z \sim 100mm$. The angle of inclination β of the B-field vector to the x-coordinate axis changes in the range $144° \le \beta \le 188°$ along the z-axis in the range $0 \le z \le 350mm$. This is shown by the B-vector graph in figure 4.8c. The B-field is twisted along the z-axis in the manner of a spiral stair case. At lower supercritical volumetric flow rates e.g. $\dot{V}_c = \dot{V}_{H1} = \dot{V}_{H2} = 110 m^3/h$ the general behaviour of the B-field on the z-axis is the same except that the intensities are reduced. The turning of the B-field vector along the z-axis is not significantly affected. This general observation is displayed in figure 4.8b and d. Here the magnetic field vector turns about the z-axis by 43° from the inner to the outer measuring position. The intensity of the B-vector is noticeably reduced. In general, in the whole range of tested supercritical flow rates $85 < \dot{V}_{H1} = \dot{V}_{H2}\,(m^3/h) < 125$ and $85 < \dot{V}_C\,(m^3/h) < 140$ the measured turning angle of the magnetic field vector along the positive z-axis varied only modestly between $40° < \beta < 45°$ along the positive z-axis.

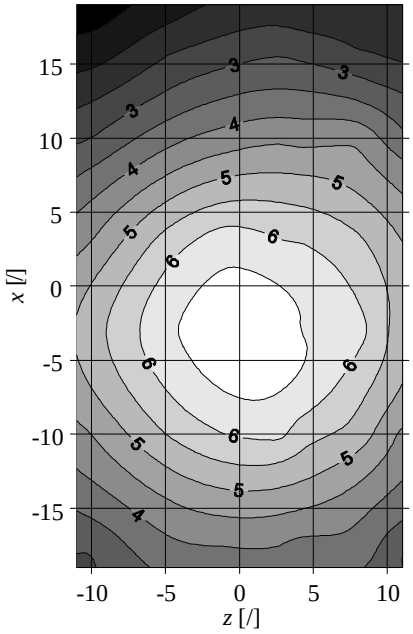

Figure 4.7: Isolines of the normal components of the magnetic field measured in the plane of the sidewise arranged vertical wood board for the conditions $\dot{V}_C = 134 m^3/h$, $\dot{V}_{H1,2} = 101 m^3/h$ and λ=*0.1 m²/s*.

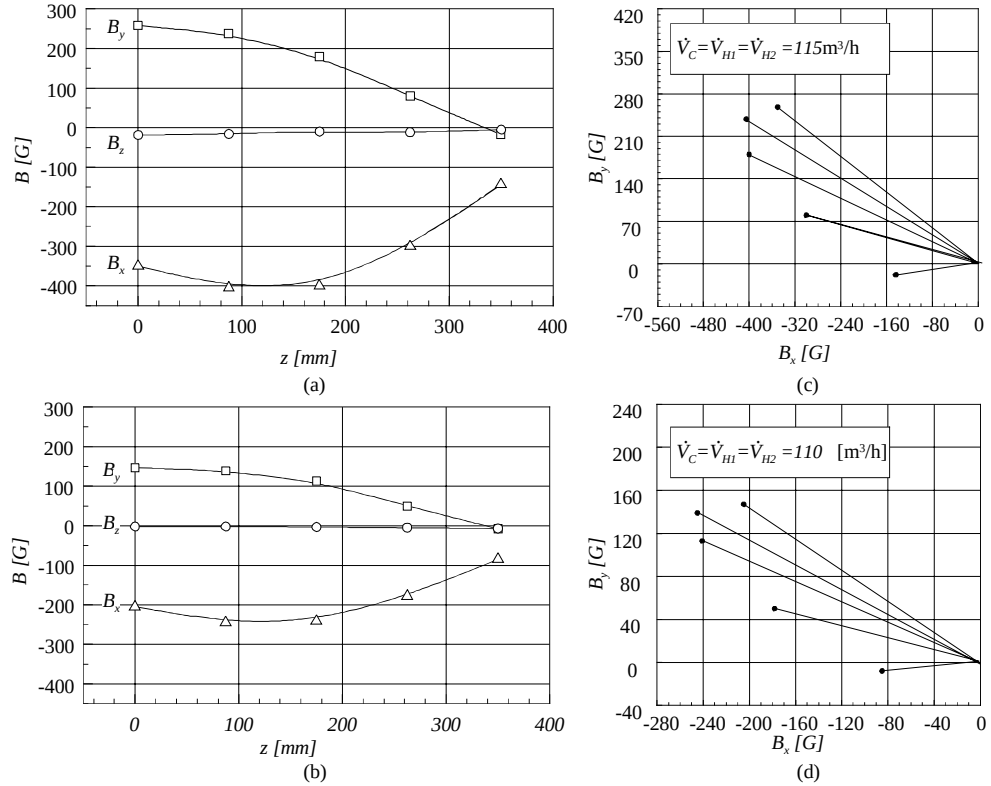

Figure 4.8: Distribution of the intensities of the magnetic field components on the module axis in the range *0≤ z(mm)≤ 350 mm* for equal volumetric flow rate: a) $\dot{V}_H = \dot{V}_C = 115\ m^3/h$; b) $\dot{V}_H = \dot{V}_C = 110\ m^3/h$; variation of the angle of inclination of the magnetic field relative to the module's position for c) $\dot{V}_H = \dot{V}_C = 115\ m^3/h$; d) $\dot{V}_H = \dot{V}_C = 110\ m^3/h$.

4.3 The effect of perturbations by external magnetic fields

We have tested the effect which an initial external magnetic field, generated by two Helmholtz coils, has on the dynamo magnetic field. The two coils are placed on both sides of the test module such that they generate an unidirectional magnetic field of quasi-dipole character penetrating the module perpendicular to its axis. The coils were operated at a DC-current of $50A$ and produced a nearly homogeneous magnetic field of about $20G$ in the module area. For tests the power for the coils was switched on or off suddenly. The direction of the external magnetic field could be changed by changing the current direction.

An interesting question is: Can saturated dynamo states of opposite field direction be established by a specific perturbation of an active dynamo state with the help of an external magnetic field? The experimental procedure for an answer is as follows. A saturated dynamo state is first produced starting from the environmental seed field by a controlled scan up of flow rates to an intermediate level of dynamo action of, say, 20-$30G$ intensity. Next, by switching on the external magnetic field of opposite direction the dynamo field is destabilised and in a transient process, lasting between several seconds up to minutes, a new saturated dynamo state of opposite field direction settles in together with the still existing external magnetic field. If the external field is switched off, a mean magnetic field of the same direction persists and a new complementary dynamo state is found. Other saturated states belonging to the same set can be generated by a suitable scan up or down of flow rates. However, the magnetic field undergoes a jump-transition to the initial dynamo state with opposite direction of the magnetic field, when the volumetric flow rates fall short of a lower bound of flow rates. The result of the outlined experimental procedure is displayed in figure 4.9. The graph shows for a fixed central flow rate of $\dot{V}_C = 112.5m^3/h$ and variable helical flow rates the saturated mean value of y-components of the magnetic field B_y on a continuous branch and the complementary isolated branch of existing stationary dynamo states. Here the field component was measured by a Hall probe at the centre of the module ($H3$, see figure 3.2). This experimental observation conforms well with the theory of imperfect bifurcations from a stationary hydrodynamic state to a stationary magnetohydrodynamic state. The lowest values of the volumetric flux for the isolated branch may be identified as a turning point from which a branch of unstable i.e. experimentally not realizable states bifurcate for higher flow rates (for more details on bifurcation theory see textbooks on hydrodynamic stability e.g. Joss & Joseph (1980)). Tilgner & Busse (2002) and Rädler et al. (2002b) calculated the stationary solutions of this branch (see figure 2.3).

Our experiments on supercritical dynamo states with field intensities larger than, say, $300G$ and with perturbations by strong external magnetic fields revealed an unexpected effect. The dynamo magnetic field, enhanced by the temporary presence of the external field, may noticeably influence the environmental magnetic seed field which determines the initial conditions for the onset of dynamo action for each sequence of stepwise rising flow rates. It so happened that, after an up-scan along a continuous branch of states and a termination of the test series at high field intensities, a subsequent test series, starting again from low subcritical flow rates, resulted in magnetic saturation fields of opposite direction on a continuous branch. A typical example is shown in figure 4.10 in form of another bifurcation graph for the B_y-component. The graph shows the continuous and the isolated branch of states.

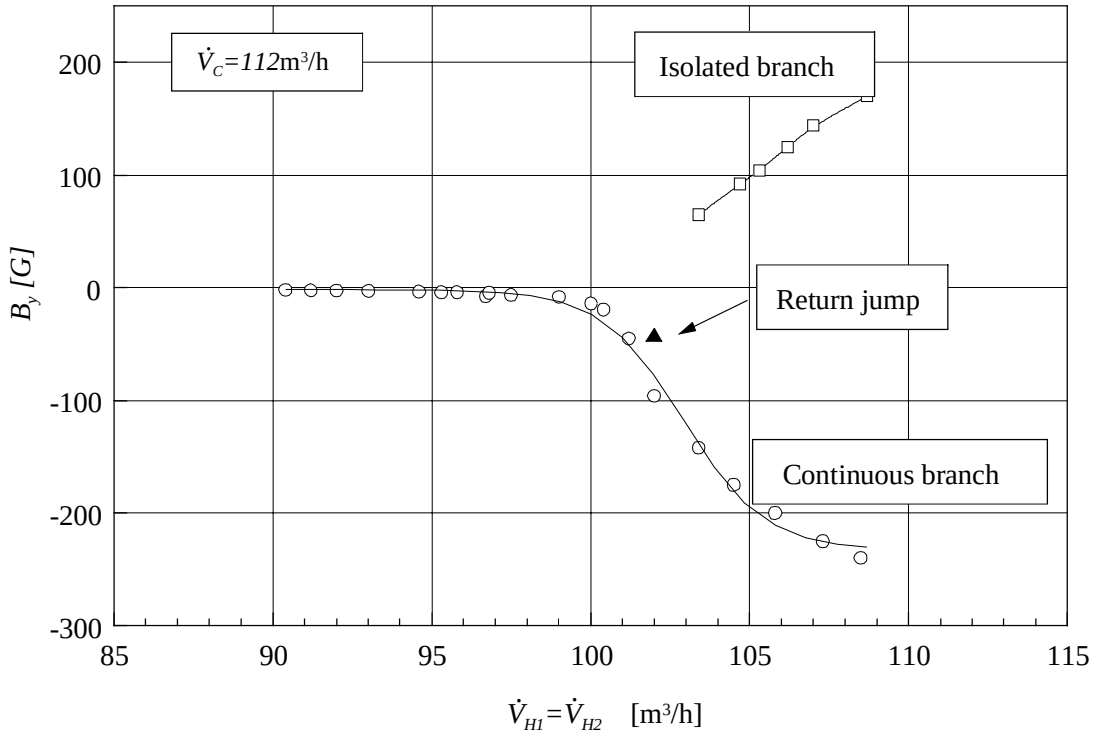

Figure 4.9: The stationary dynamo states at supercritical conditions represented by the measured local B_y-component. The graph shows two sequences of stationary states, one set on a continuous branch and another set on an isolated branch. The return jump from the isolated branch to the continuous branch is indicated by the symbol ◄. Parameter range: $\dot{V}_C = 112\ m^3/h$, $92 < \dot{V}_{H1,2}\ (m^3/h) < 110$.

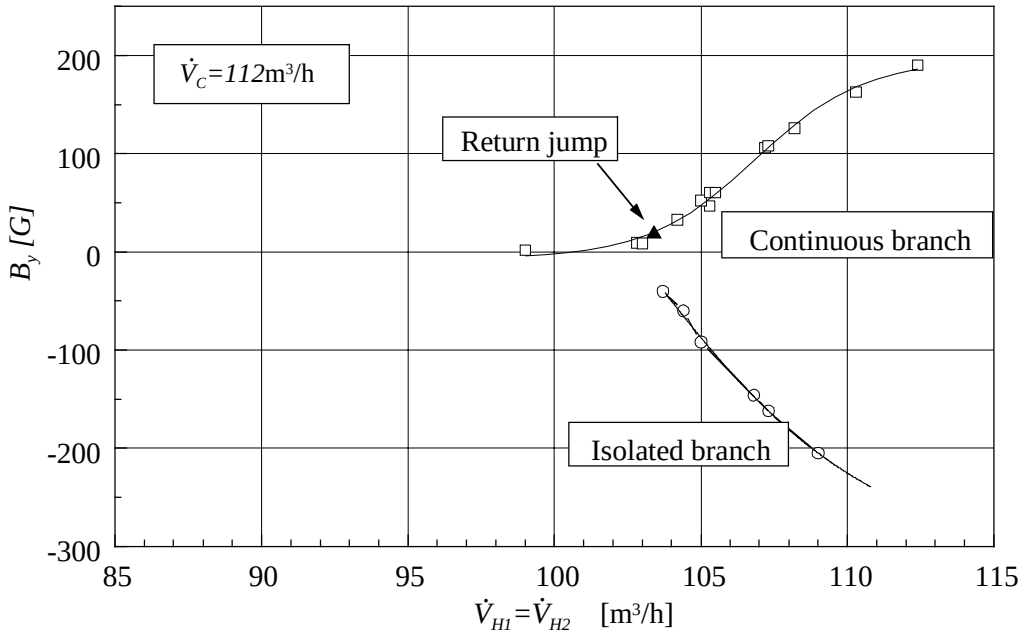

Figure 4.10: Stationary dynamo states on a continuous and an isolated branch of a bifurcation graph, however, compared to figure 4.9 the branches are reversed due to a modification of the environmental seed magnetic field by the dynamo magnetic field of the preceding experiment. Parameter range: $\dot{V}_C = 112\ m^3/h$, $98 < \dot{V}_{H1,2}\ (m^3/h) < 113$.

The character of the complementary isolated branch could only be assured in a test series, if the transitions from the continuous to the isolated branch and reverse are triggered by an external perturbation at an intermediate intensity level of the dynamo and the external magnetic field, say in the range $50 \leq |B|(G) \leq 200$. If a transition is enforced at high intensity levels of dynamo action ($|B| > 300\ G$) the complementary dynamo states of opposite direction can be scanned down in a continuous manner to vanishing field intensities. This is demonstrated in figure 4.11. More details are given in the graph and the figure caption. The explanation of this behaviour has to be associated with the impact of high intensity magnetic fields on the steel structures of the laboratory building. Indeed, although the seed magnetic field level proved to be always of the order of the Earth's magnetic field, i.e. $|B_E| \sim 0.5G$, measurements done with a carry-on Gauss meter show that the orientation of the seed magnetic field near the dynamo module is nearly perpendicular to the orientation of the Earth's magnetic field measured outside the building.

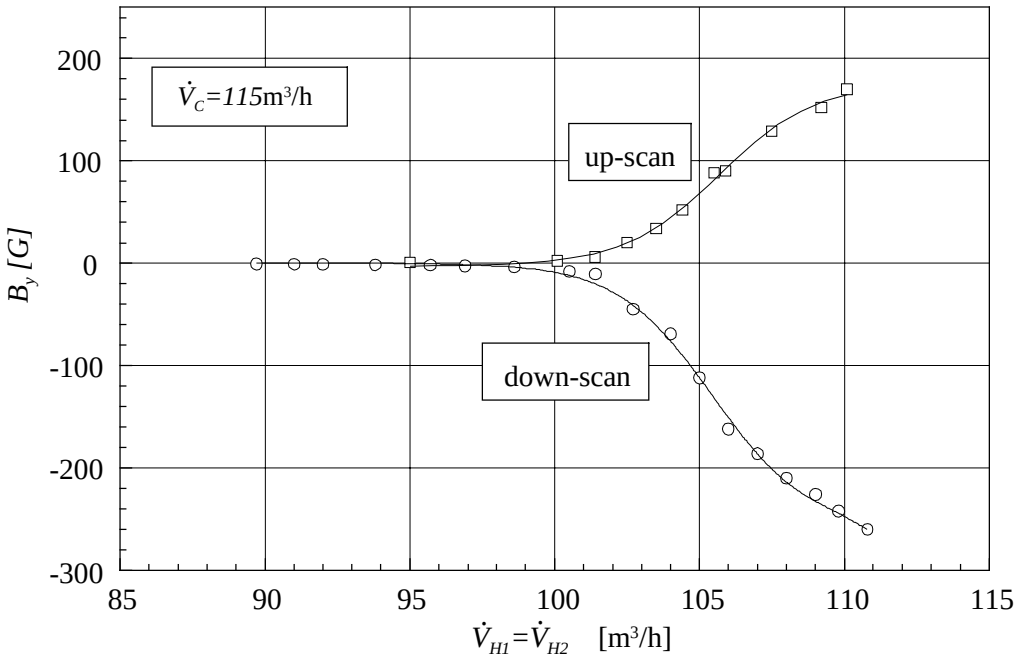

Figure 4.11: Stationary dynamo states continuously connected to hydrodynamic states for both directions of the magnetic field. The states were obtained in a monotonic up- and down-scan with a switch over to the other branch at high magnetic field intensities. It is suggested that the change of the field direction at high field intensity modifies the environmental seed field by changing the remanent week ferromagnetism in the steel structures of the laboratory building. Parameter range: $\dot{V}_C = 115 m^3/h$, $89 < \dot{V}_{H1,2}\,(m^3/h) < 130$.

Moreover, measurements of the seed magnetic field along the module axis by traversing the Hall probe show a distinct but small change for the measured data before and after dynamo tests. This can be seen in figures 3.3a,b and 4.12a,b. This observation supports our conjecture that dynamo action of high enough intensity may modify the seed field and thus result in different saturated solutions.

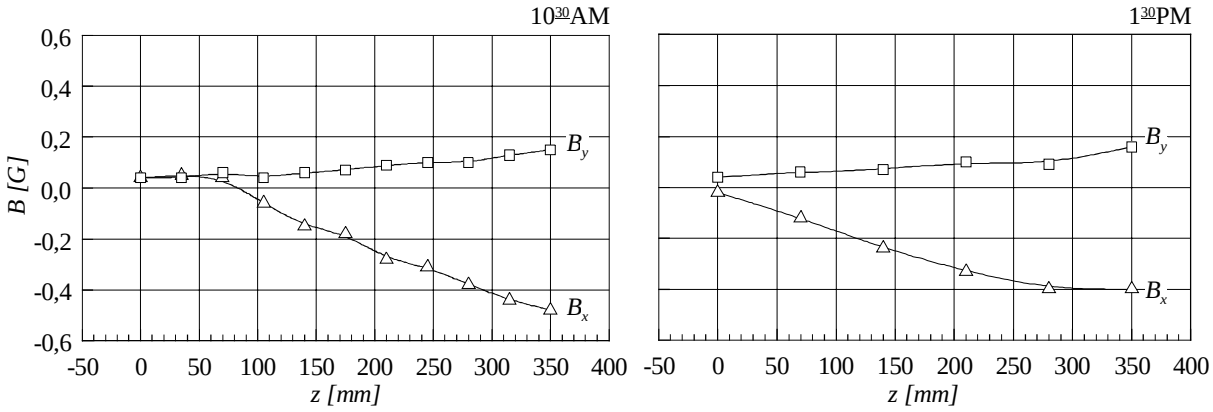

Figure 4.12: The measured seed magnetic field at low sub-critical volumetric flow rates $\dot{V}_H = \dot{V}_c = 77.5\ m^3/h$ before (a) and after (b) a measuring campaign with dynamo action of high intensity, i. e. $|B| \sim O(400\ G)$.

4.4 The effect of non-symmetric helical flow rates

The dynamo test facility can be operated with different flow rates in the three independent channel systems of the test module. We investigated the influence of a non-symmetric velocity distribution on the structure of the dynamo magnetic field by feeding, e.g., one helical loop with a flow rate $\dot{V}_{H1} = 85\ m^3/h$ and the second helical loop with $\dot{V}_{H2} = 115\ m^3/h$ and vice versa at a constant flow rate of $\dot{V}_c = 128\ m^3/h$ in the central loop. The change in the magnetic field structure was qualitatively checked by the orientation of the compass needle array on the side board and the recordings of the traversable Hall probes. Figure 4.13 shows the distribution of intensities of the field components along the semi-axis of the module. Three situations are displayed by the graphs in figure 4.13: the distribution (a) for equal helical flow rates $\dot{V}_{H1} = \dot{V}_{H2} = 100 m^3/h$, (b) for non equal helical flow rates $\dot{V}_{H1} = 85\ m^3/h$, $\dot{V}_{H2} = 115\ m^3/h$ and for the complementary case (c) $\dot{V}_{H1} = 115\ m^3/h$, $\dot{V}_{H2} = 85\ m^3/h$. The first observation is, that even significantly different flow rates lead to steady mean fields. There is an obvious tendency that the intensities of the *x*- and *y*-components of the magnetic field for the non-symmetric flow rates are larger than for the symmetric case. i.e. equal helical flow rates. Moreover, the non-symmetric cases do not achieve the same intensity values. The case for $\dot{V}_{H1} = 115\ m^3/h$, $\dot{V}_{H2} = 85\ m^3/h$ shows significantly higher intensities compared to the case $\dot{V}_{H1} = 85\ m^3/h$, $\dot{V}_{H2} = 115\ m^3/h$. The reason for this is not clear. It is conjectured, that this effect is caused by certain structural non-symmetries in the module such as the particularities of the feeding piping system connected to the module and inhomogeneities of the seed magnetic field due to the steel structures of the laboratory building. The main difference compared to the flow situation with equal helical flow rates is the largely enhanced z-components of the magnetic field shown in figure 4.13b,c. Depending on the shift of the helical flow rates from the reference case positive or negative field components B_z occur. This indicates that the axis of the reference magnetic field B inclined to one or the other direction of the module axis.

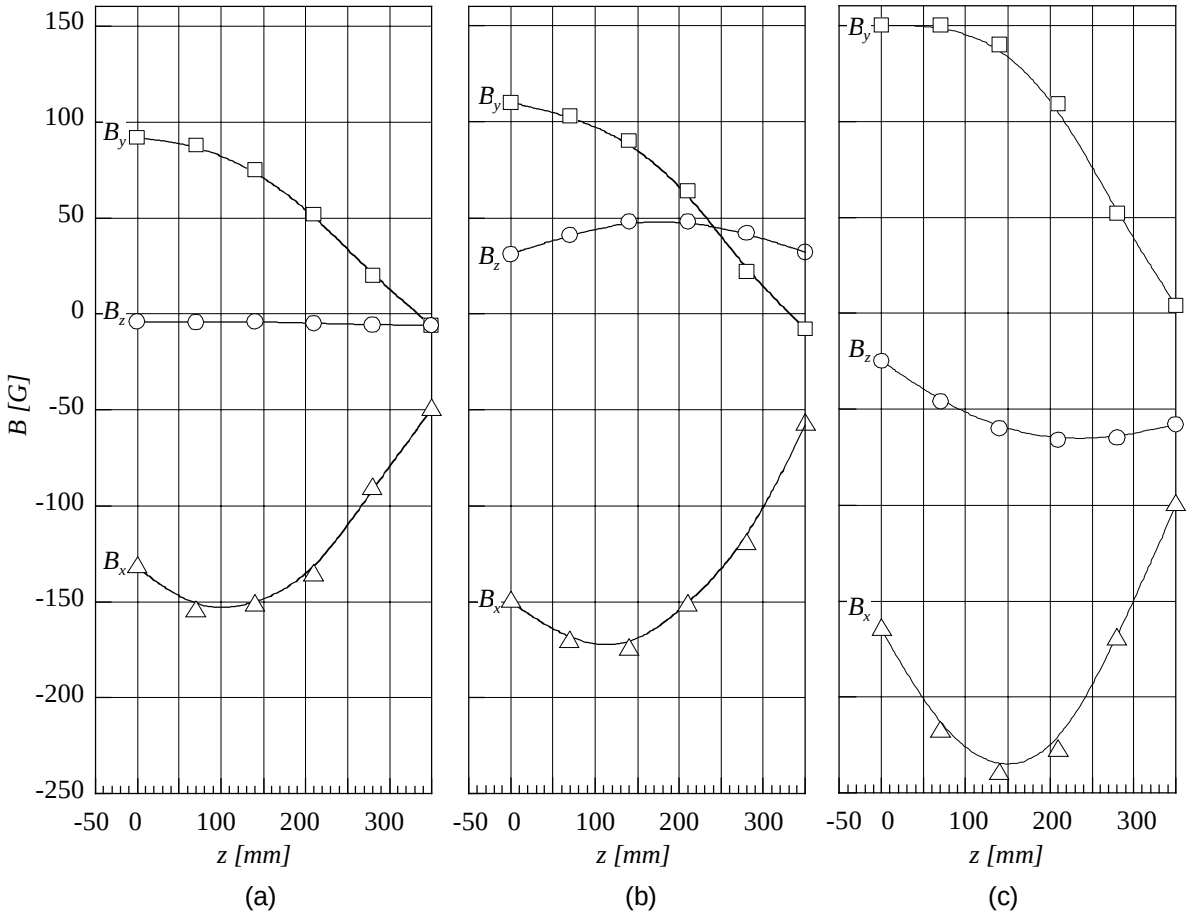

Figure 4.13: Distribution of the magnetic field components along the axis of the module in the range $0 \le z \le 350$ mm for symmetric and non-symmetric flow distributions. (a) $\dot{V}_{H1} = \dot{V}_{H2} = 100\ m^3/h$, $\dot{V}_C = 128\ m^3/h$; (b) $\dot{V}_{H1} = 85\ m^3/h$, $\dot{V}_{H2} = 115\ m^3/h$, $\dot{V}_C = 128\ m^3/h$; (c) $\dot{V}_{H1} = 115\ m^3/h$, $\dot{V}_{H2} = 85\ m^3/h$, $\dot{V}_C = 128\ m^3/h$.
Legend: $\Delta \rightarrow B_x$, $\square \rightarrow B_y$, $O \rightarrow B_z$.

4.5 Temporal features of saturated dynamo states

The saturated dynamo states are steady in the time average, but, fluctuate about a mean value of the magnetic field. For characterizing these turbulent fluctuations long term recordings of the magnetic field components (B_x, B_y, B_z) of a duration between $1200s$ up to $4800s$ were taken using the Hall probes. A listing of all combinations of flow rates of long term recordings is displayed in figure 4.14. A typical recording for volumetric flow rates $\dot{V}_c = \dot{V}_{H1} = \dot{V}_{H2} = 115\ m^3/h$ is shown in figure 4.15a. An extended intersection is shown in figure 4.15b. From the time signal of figure 4.15b two quasi-periodic features can be recognized. There are fluctuating events of a frequency of about $3\ Hz$ and $35\ Hz$.

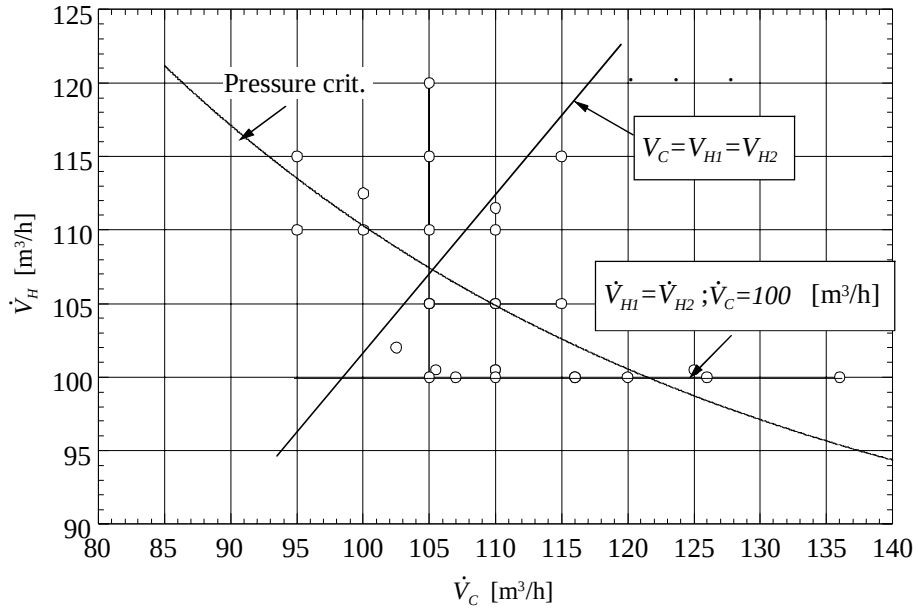

Figure 4.14: Combinations of volumetric flow rates of long time signal recording experiments.

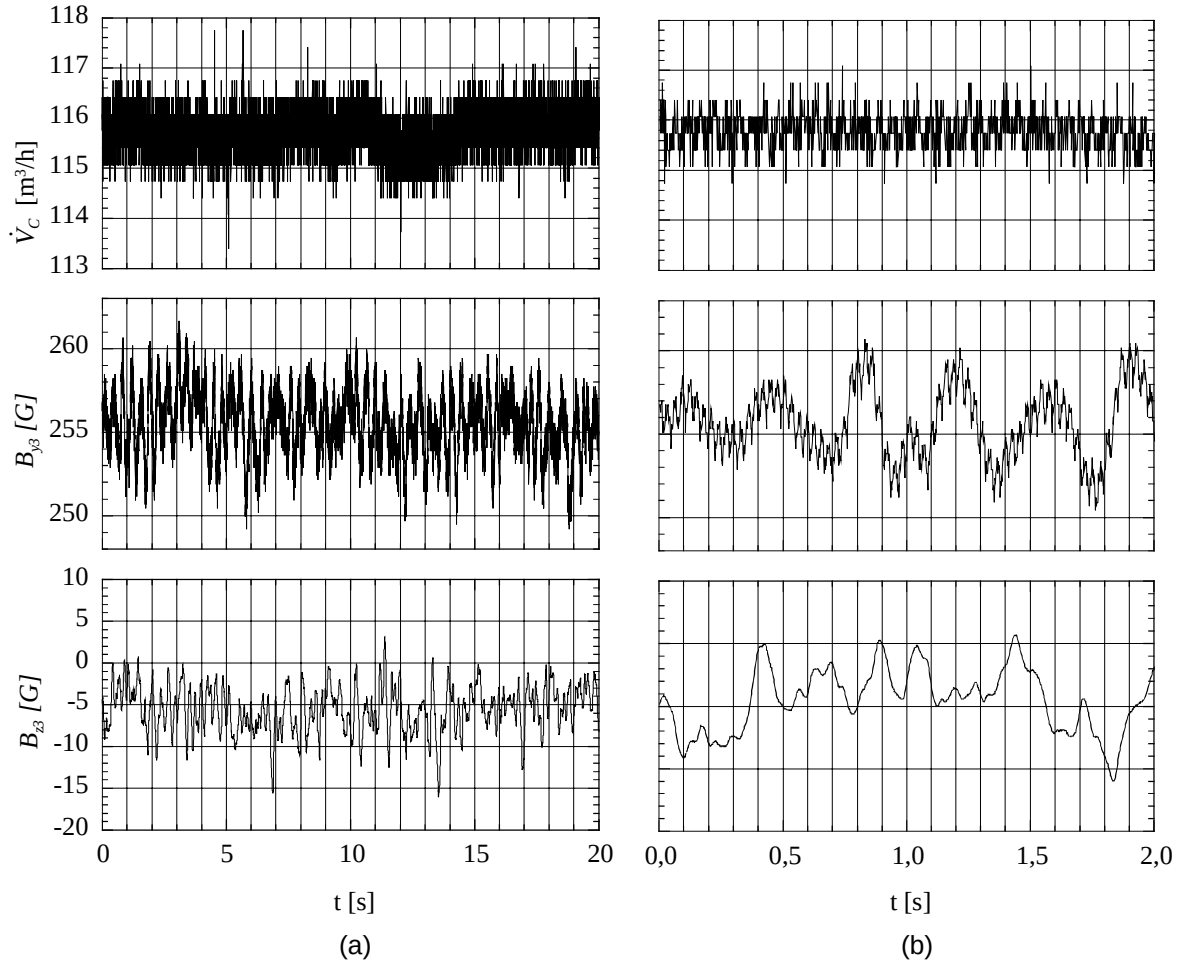

Figure 4.15: Typical time signals of the volumetric flow rate and two components of the magnetic field (B_y, B_z) recorded by the Hall-probe *H3* for constant volumetric flow rates $\dot{V}_C = \dot{V}_{H1,2} = 115\ m^3/h$ at *z=0*. (a) time interval *20s*; (b) time interval *2s*.

We shall identify these frequencies in the power density spectra (*PDS*) later. The quality of the fluctuations may be judged from the probability density function (*PDF*) and the first three moments, the square root of the variance (*RMS*), the skewness and flatness. Figure 4.16 shows a typical *PDF*-function for the recording in figure 4.15.

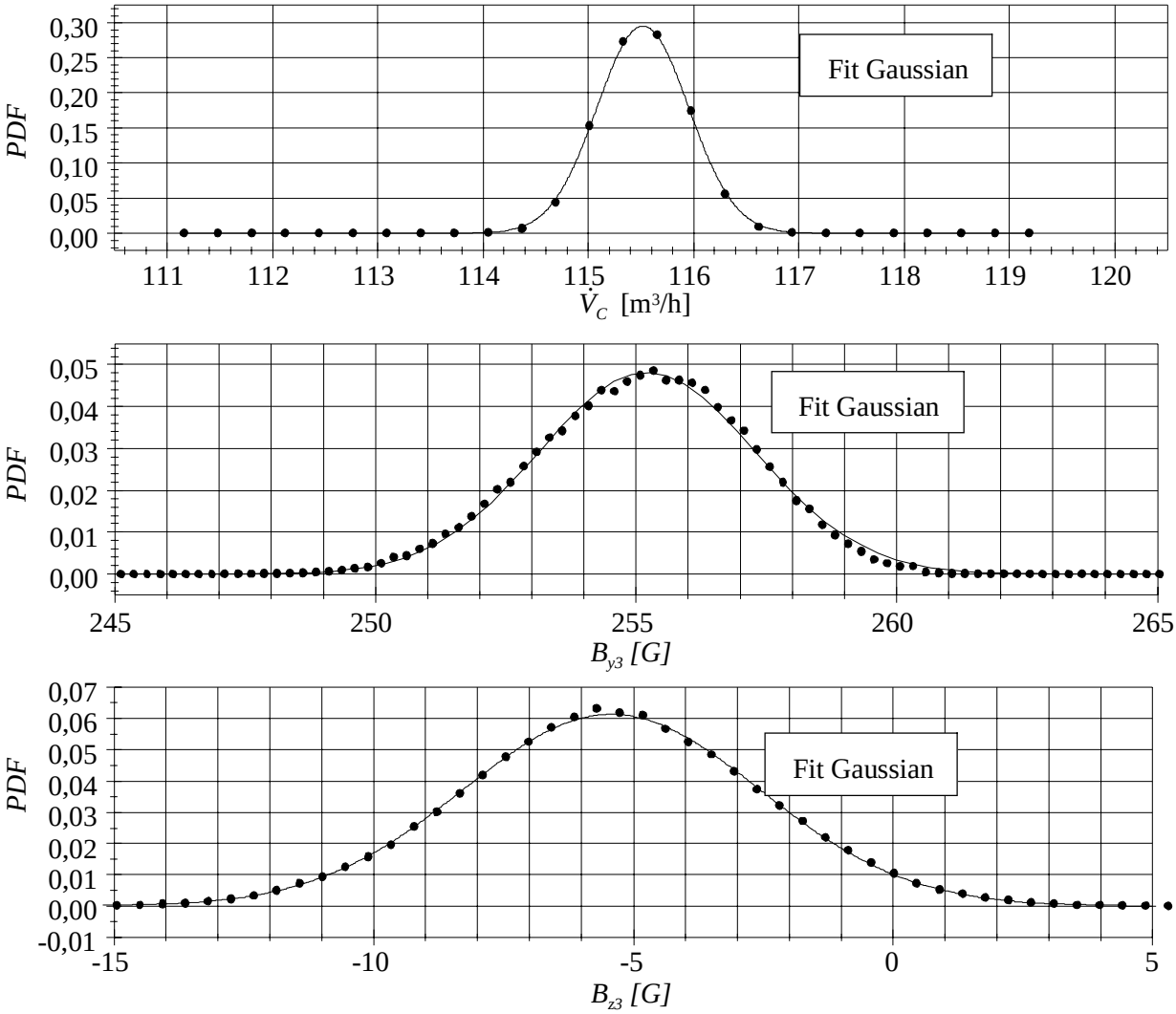

Figure 4.16: Probability density function (*PDF*) of the time signals of the volumetric flow rate and the two components of the magnetic field (B_y, B_z) of the Hall-probe *H3* for constant volumetric flow rates $\dot{V}_C = \dot{V}_{H1,2} = 115\ m^3/h$ at $z=0$.

The associated higher moments of the component of the magnetic field B_y are shown in figure 4.17 for a recording period of *1000 s*. The moments in this figure were evaluated for periods of 10s and for signal recording rates of *512 Hz*. The characteristic features are the quasi-Gaussian *PDF* with a vanishing skewness, a constant flatness of *2.5* and a constant *RMS* value $b_y^*=0.58G$. The latter has to be compared with the mean value $B_y=260G$ which gives a small relative fluctuation level of about *0.25 %*. It has been observed, that this level is larger for the *z*-component B_z and for all components near the onset of self-excitation. Thus, the graph 4.17 indicates that characteristic turbulence properties are constant at saturation.

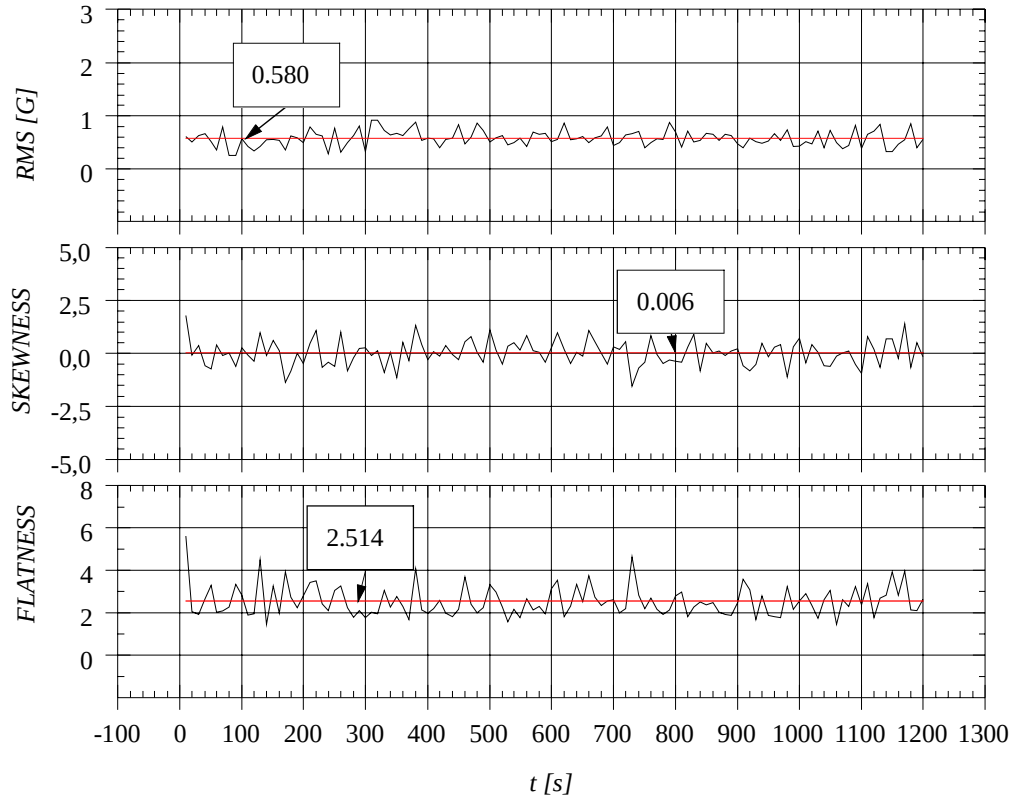

Figure 4.17: The square root of the variance (RMS), skewness and flatness values of time signal $B_y(0,0,0,t)$ of Hall-Probe $H3$ at $z=0$ for the flow rates $\dot{V}_C = \dot{V}_{H1,2} = 115\ m^3/h$.

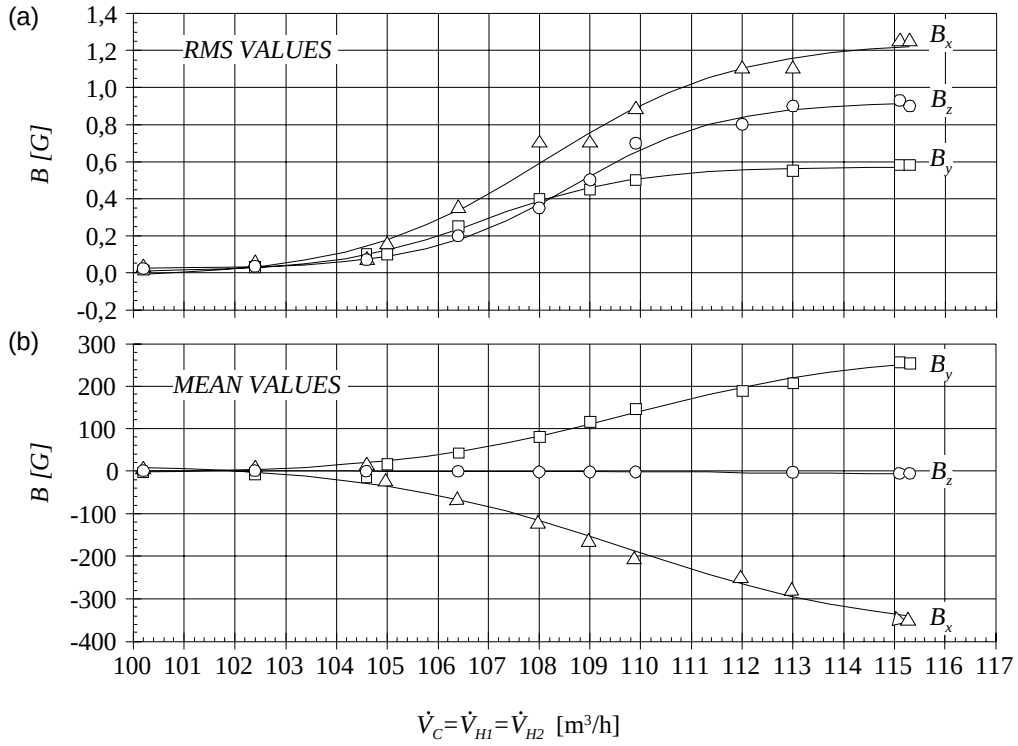

Figure 4.18: The square root of the variance (RMS values) and the associated mean values for the time signals of Bx, By, Bz as a function of the flow rates. (a) RMS-values; (b) the associated mean values.

RMS values were also evaluated for other lower and equal flow rates ($\dot{V}_{H1} = \dot{V}_{H2} = \dot{V}_C$). They are shown in figure 4.18 together with the associated mean values of the magnetic field. The tendency towards a sub-linear increase of the *RMS* values of B_x, B_y, B_z for higher flow rates in graph 4.18a is significantly stronger than that of the mean values in graph 4.18b. In particular B_y and B_z seem to achieve saturation levels for $\dot{V} > 112 m^3/h$. This feature can be quantified by normalising the *RMS* value by the corresponding mean values. The normalised *RMS* values clearly decrease with increasing flow rates. From this observation we may conjecture, that the increasing intensity of the mean magnetic field limits the growth rate of the turbulent fluctuations of the field.

Further insight into the character of the fluctuations is gained by considering their power spectral density (*PDS*). Spectra for *y*- and *z*-components of the magnetic field for five choices with equal volumetric flow rates $\dot{V}$ = 95 m^3/h, 102 m^3/h, 106 m^3/h, 110 m^3/h and 115 m^3/h are displayed in figure 4.19a and b. Spectra for the *y*-component for the fixed flowrate $\dot{V}_{H1,2}$ = 100 m^3/h and for five variable central volumetric flow rates $\dot{V}_C$ = 106 m^3/h, 116 m^3/h, 120 m^3/h, 125 m^3/h and 136 m^3/h are displayed in figure 4.19c. The spectra were obtained from long time Hall probe recordings in the centre of the module (probe position *H3*, see figure 3.2). We consider figure 4.19a. According to our criterion for onset of self-excitation, as sketched in figure 4.4, the flow rate $\dot{V}$ = 102 m^3/h is sub-critical and the flow rates $\dot{V}$ = 110 m^3/h and 115m^3/h are supercritical. The spectra of the two super-critical states show the following characteristic features: the spectra exhibit three distinct ranges of power distribution, a lower frequency range $0.1 < f(Hz) < 3$ with nearly constant power for the B_z-fluctuations and a dependence on the frequency like $\sim f^{-1}$ for the B_y-fluctuations.In the range $3 < f(Hz) < 20$ the spectral power decays nearly as $\sim f^{-3}$ and beyond this range the power decays even more rapidly in particular for the higher flow rate $\dot{V}$ = 115m^3/h nearly as $\sim f^{-5}$ or even more strongly[4]. The transition from the first to the second range is distinctly marked by a cut-off frequency in the spectrum of the B_z-component and a broad but distinct power peak in the B_y-power spectrum. The centre of this power peak shifts to lower frequencies for lower supercritical flow rates. It becomes broader and less pronounced and disappears completely when critical conditions are approached. In our specific case the power peak frequency reduces from *2.7Hz* to about *1.2Hz*. A similar effect is seen in figure 4.19c for volume flow rates $\dot{V}_{H1} = \dot{V}_{H1} = 100 m^3/h$ and variable $106 \le \dot{V}_C\ [m^3/h] \le 136$. We shall return to this observation later in the general discussions. For the sub-critical case a broad band spectrum without particular features in the B_y spectra but with some indication for a cut off-frequency in the B_z spectrum is observed. These observations for a test sequence of equal volumetric flow rates have been confirmed for other supercritical tests listed in figure 4.14. We conducted also some experiments at sub-critical volumetric flow rates under the influence of an external magnetic field of about *20G* generated by the Helmholtz coils. The typical results for the power spectral density of the magnetic field fluctuations is shown in figure 4.19a for equal flow rates $\dot{V}_{H1} = \dot{V}_{H2} = \dot{V}_C = 95 m^3/h$. The power spectrum is comparable with the spectrum for volumetric flow rate $\dot{V}_{H1} = \dot{V}_{H2} = \dot{V}_C = 102 m^3/h$ but without external magnetic field. As a further example the spectra of the field components B_x, B_y, B_z for the volumetric flow rates $\dot{V}_C = 105 m^3/h$, $\dot{V}_{H1,2} = 120 m^3/h$

[4] The power spikes in the spectrum for higher frequencies f>30 Hz are associated with experimental noise originating from the general power supply for the test rig by the 50 Hz AC grid and the 30 Hz tyristor controlled power supply for the MHD-pumps.

and the flow rates $\dot{V}_C$ =115m^3/h, $\dot{V}_{H1,2}$ =105 m^3/h are presented in figure 4.20.The first example is in the distinctly super critical regime, the second one is also in a supercritical state but close to the margin of self-excitation.

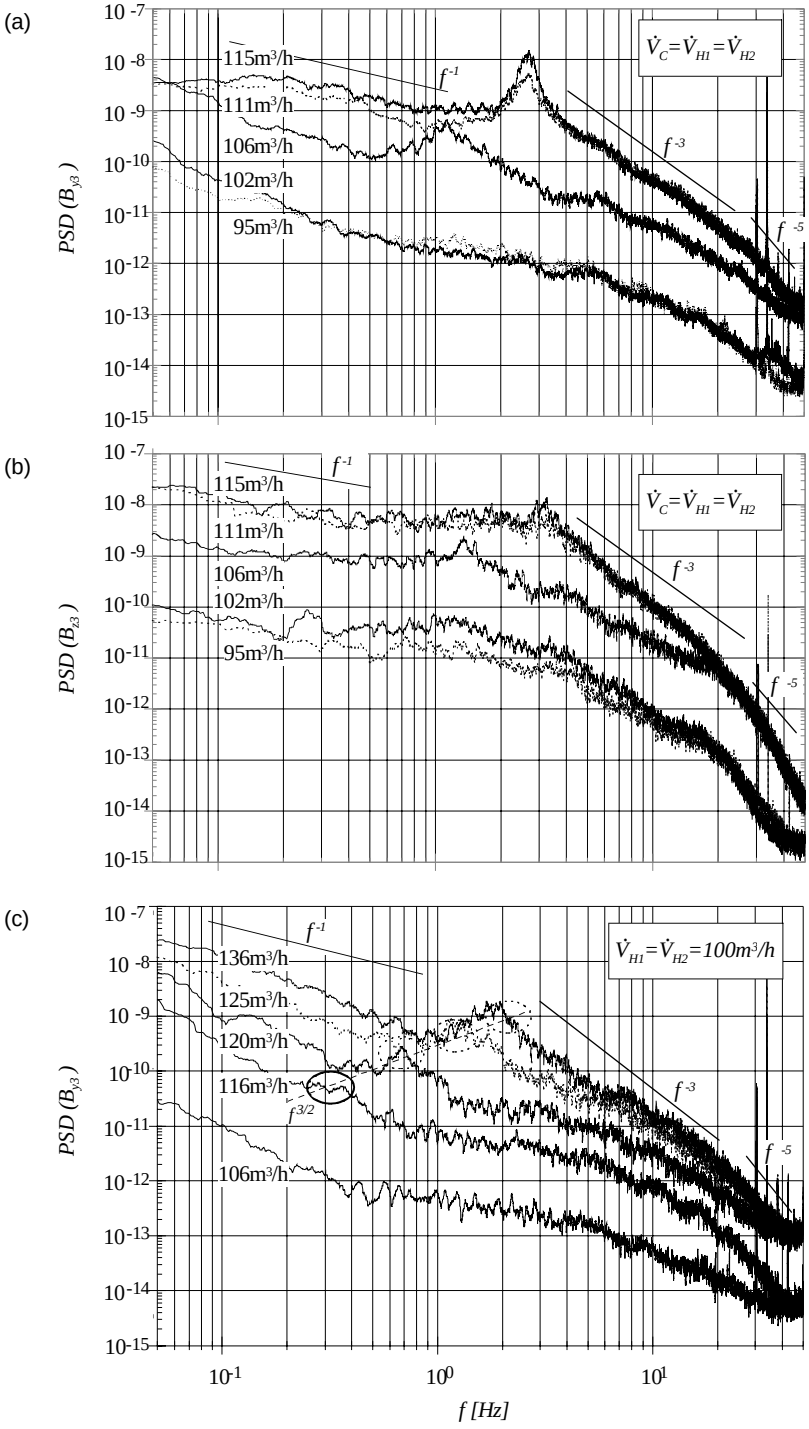

Figure 4.19: Power spectral density (*PSD*) for the components B_x, B_y, B_z for five different volumetric flow rates of operation at the position *z=0* of Hall-probe *H3*. (a) *PSD* for the B_y-component for five equal volumetric flow rates $\dot{V}$ =*95, 102, 106, 111* and *115*m^3/h; (b) *PSD* for the B_z-component for five equal volumetric flow rates $\dot{V}$ = *95*, *102*, *106*, *111* and *115*m^3/h; (c) *PSD* for the B_y-component for $\dot{V}_{H1}=\dot{V}_{H2}=100m^3/h$ and for five central volumetric flow rates $\dot{V}_C$ = *106*, *116*, *120*, *125* and *136*m^3/h.

Aside from the long time recordings in the centre of the module, measurements were also performed on the module axis in the range $0 \le z(mm) \le 350$ in five equidistant positions. Complementary to the previous spectra of the centre position we present in figure 4.21 some power spectra of the components B_y and B_z evaluated from signal recordings at the locations $z=0, 85, 175, 350\ mm$ for the case of equal volumetric flow rates $\dot{V} = 115\ m^3/h$. The spectra of B_z–component at $z=175\ mm$ and $z=350\ mm$ exhibit a broad band behaviour with the same distinct ranges of power decrease as in the previously discussed cases namely as $\sim f^{-1}$ in the range $f \le 2Hz$, in the range $2 \le f \le 30Hz$ as $\sim f^{-3}$ and less than $\sim f^{-5}$ in the range $f > 30\ Hz$. The spectra of the B_y–component reveals the characteristic power peak in the range $f \sim 2\text{-}3\ Hz$ and for positions $z < 170\ mm$. However, the power peak broadens and decreases with growing distance from the centre and disappears in the spectrum near the boundary of the module i.e. at $z = 350\ mm$. Simultaneously the characteristic power ranges get blurred. This behaviour is attributed to the decrease of the mean magnetic field intensity with increasing distance from the centre.

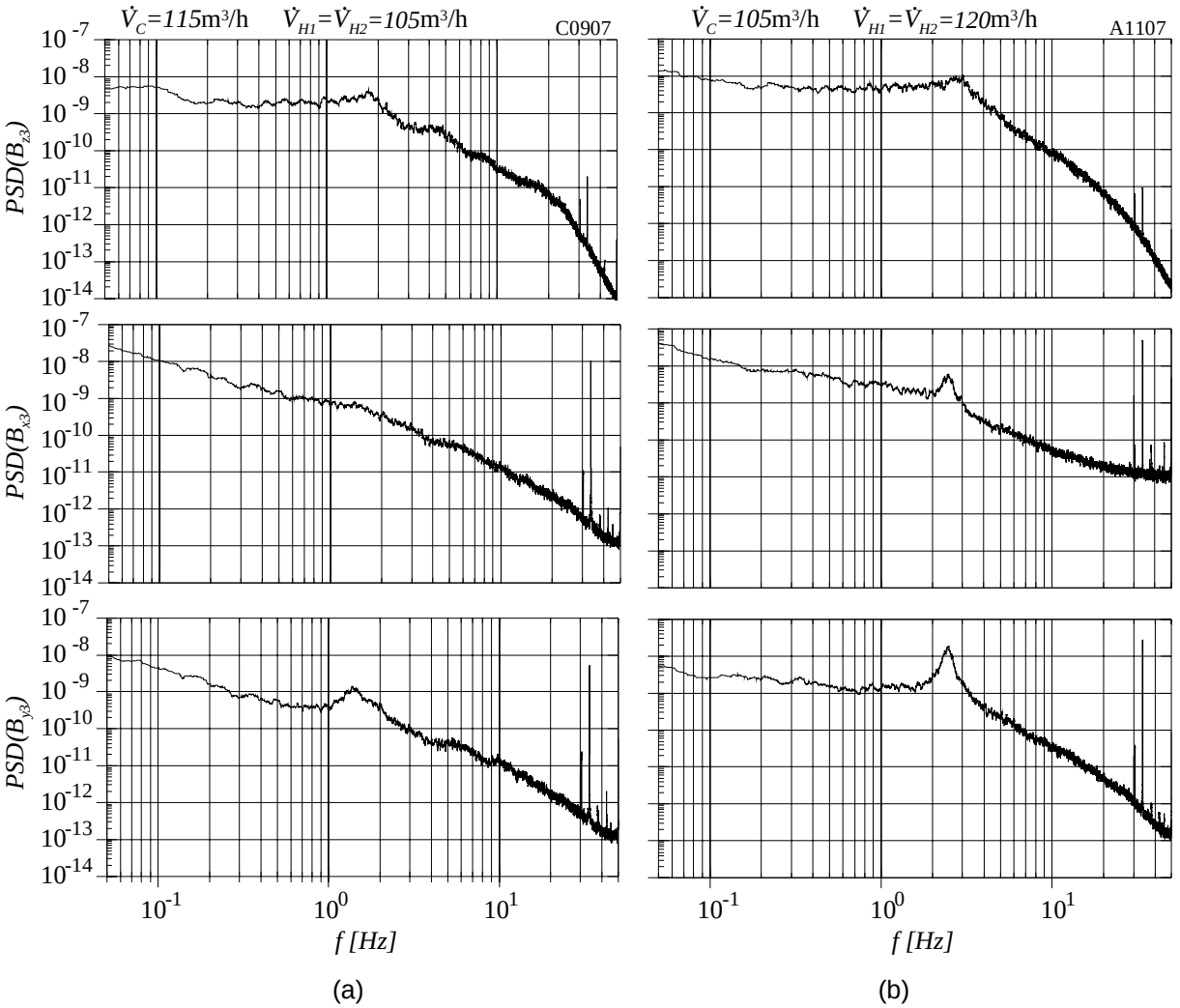

Figure 4.20: Power spectral density functions for the components B_x, B_y, B_z for two different volumetric flow rates of operation. (a) $\dot{V}_C = 105m^3/h$, $\dot{V}_{H1,2} = 120m^3/h$; (b) $\dot{V}_C = 115m^3/h$, $\dot{V}_{H1,2} = 105m^3/h$.

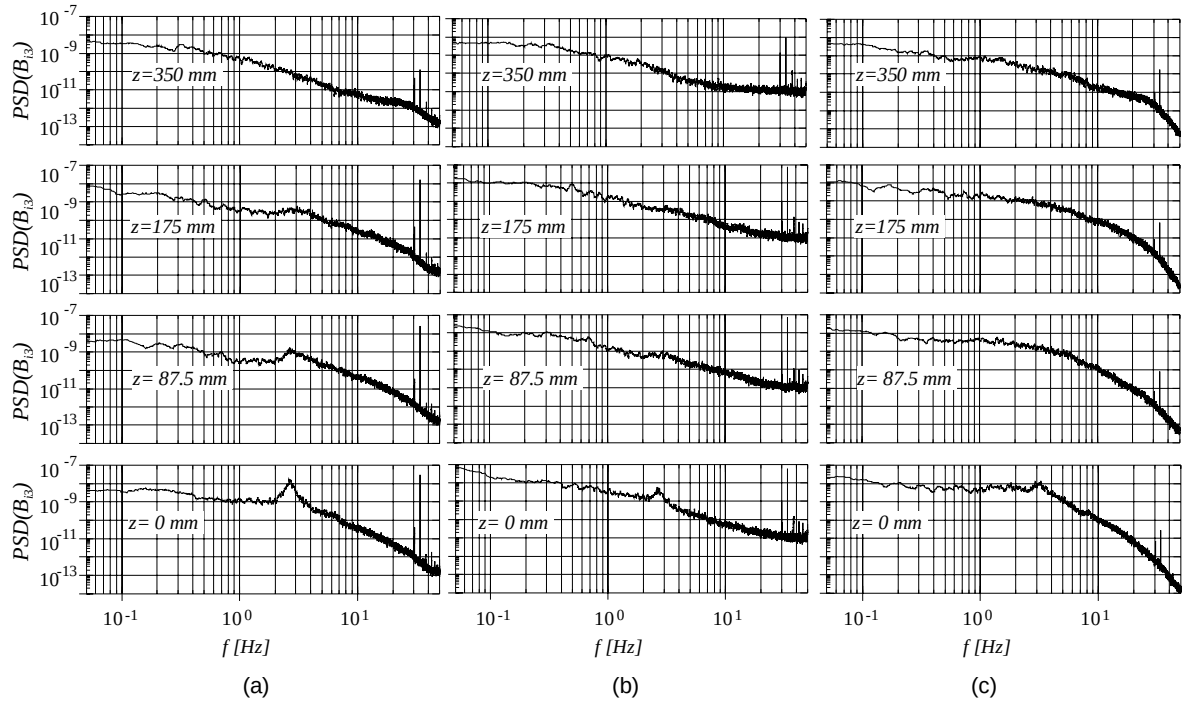

Figure 4.21: Power spectral density (PSD) of the components B_y, B_x, B_z of Hall-probe H3 for volumetric flow rates $\dot{V}_C = \dot{V}_{H1,2}$ *=115m³/h* and at the positions $\vec{X}$ =(*0, 0, 0mm),* X =(0, 0, *87.5mm*), X =(0,0,*175 mm*), X = (*0, 0, 350 mm*). (a) B_y ; (b) B_x and (c) B_z.

Dynamic regularities of the magnetic field can also be identified by evaluating auto-correlation (*ACF*) and cross-correlation functions (*CCF*) of the time signals. In particular cross-correlation functions (*CCF*) may serve as a tool to detect the spatial coherency of time signals recorded at different locations. Such *CCF's* have been evaluated from Hall probe signal recordings. Typical sets of *CCF's* for time series of B_y-signals from the Hall probes *H3* and *H4* are displayed in figures 4.22a, b, c for the volumetric flow rate combination $\dot{V}_C = \dot{V}_{H\ 1,2}$*= 115m³/h*. Each figure shows five *CCF* graphs associated with five different positions of the two probes as they are simultaneously traversed along the module axis at a constant distance from each other. The set of *CCF's* is presented in different time intervals ranging from $-400 < \tau(s) < 400$ in figure 4.22a to $-4 < \tau(s) < 4$ in figure 4.22c.

All *CCF's* exhibit two characteristic features: 1) a base caused by correlated low frequency events, 2) a narrow band peak of highly correlated high frequency fluctuations. The first feature can be identified in all *CCF* graphs of figure 4.22a as a peaky bulge at location $\tau = 0$ which is large and positive at the outermost position of the two probes (*H4* at $z = 215$ *mm*, *H3* at $z = 350$ *mm*) and small and even negative at the innermost position (*H4* at $z = -135$ *mm*, *H3* at $z = 0$ *mm*). The transition from the negative to the positive correlation peak at $z = 0$ *mm* can be explained by the traversing of the two probes through a B_y-field with a maximum near the position $z \approx -0$ *mm* (see figure 4.8b) and a varying gradient. Accordingly the low frequency time signals of the two probes may be in phase or in opposite phase resulting in a positive and negative "pointed cap" peak of the correlation curve.

The time scale of the low frequency correlation base may be estimated by the intersection of the tangent line to the cap peak with the abscissa as indicated in figure 4.22a (B_{y3}: z = *265.5mm*, B_{y4}: z = *127.5mm*). The estimate is $\tau \approx 50–100$s which corresponds to a low frequency event of $f \approx 0.02–0.01Hz$.

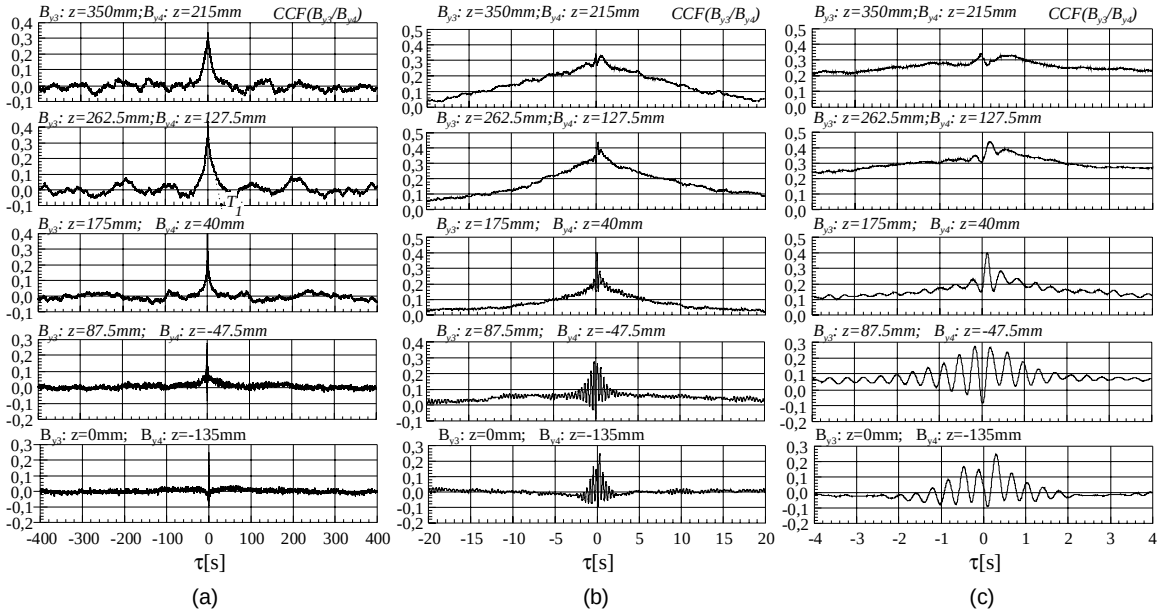

Figure 4.22: Cross-correlation function (*CCF*) obtained from B_y-recordings of Hall probes *H3* and *H4* at different positions on the module axis in the range $-135 < z_{H4}(mm) < 365$, $0 < z_{H3}(mm) < 350$; displayed time intervals. (a) $-200 < \tau(s) < 200$; (b) $-20 < \tau(s) < 20$; (c) $-5 < \tau(s) < 5$. Experimental condition: $\dot{V}_C = \dot{V}_{H1,2} = 115 m^3/h$, $\lambda = 0.1 m^2/s$.

The other feature, the narrow band oscillatory behaviour of the *CCF* near $\tau = 0s$ (which is particularly pronounced for Hall probe locations near the centre of the module) is well recognized in figure 4.22b. The character of the *CCF's* in the near centre range reflects the properties of the power density spectra near their power peaks (see figure 4.19 and 4.20). The frequency of the power peak is directly related to the oscillatory period in the *CCF* (e. g. for B_{y3}: z = *0mm*, B_{y4}: z= *-135mm* one reads in figure 4.22c the value $\tau \approx 0.3s$ and correspondingly in figure 4.19 the value $f \approx 2.8Hz$). The band width of the power peak in figure 4.19 is correlated to the decay time scale of the corresponding *CCF*. It may be assessed as $\Delta f \approx 1s$. The associated decay time scale (indicated in figure 4.22) is $\tau \approx 1–2s$. (For more general information on signal analysis see e. g. Bendat & Piersol (1986)). In principle the *CCF's* should also indicate a transit time of wave-like events passing in a more or less regular time sequence the spatially separated probes. Indeed, for the measurements near the module centre a very small signal transit time of $\Delta\tau \approx 0.1s$ between the positions z = *0mm* and z = *-135 mm* may be conjectured. However, so far the evaluated *CCF's* did not give unbiased results for a delay time in the whole range of oscillatory behaviour of the *CCF* near $\tau = 0s$. A more precise evaluation of transit times would require new Hall probe measurements with higher temporal resolution and variable spacing between the traversable sensors.

Cross-correlation measurements between Hall probes at large distance, i. e. between positions *H5* or *H6* and *H3* or *H4* have shown only week correlation of about *10%* in a very low frequency range $f < 0.03Hz$. In all evaluated cases no delay time could be observed. This indicates that the low frequency events occurred at both measuring positions simultaneously. A typical *CCF* for this kind of correlation measurement is shown in Figure 4.23.

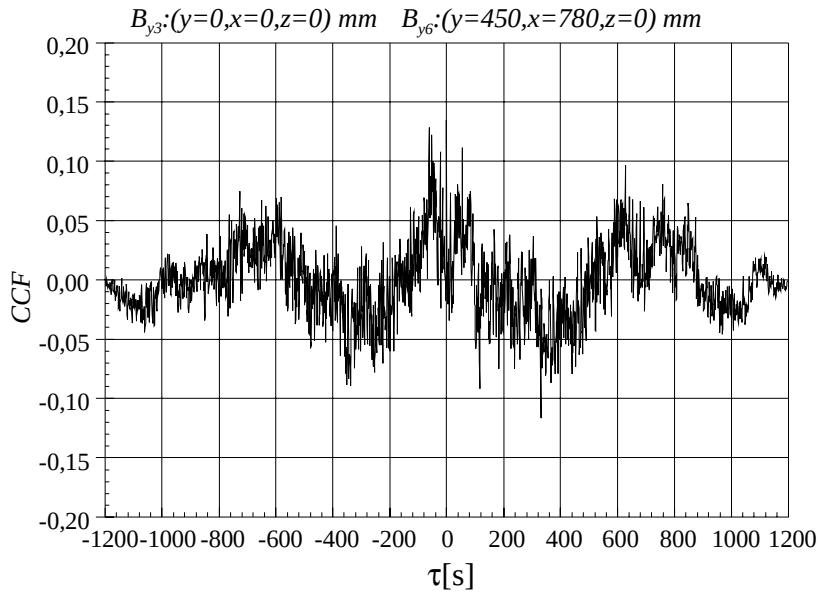

Figure 4.23: Cross-correlation function (CCF) obtained from signal recordings of Hall probes at positions H3 and H6. Experimental condition: $\dot{V}_C = \dot{V}_{H1,2}$ = 115 m^3/h, λ= 0.1m^2/s.

5 Discussions

In order to facilitate the discussions we have evaluated relevant magnetohydrodynamic parameters for some characteristic experimental conditions. Such parameters are the fluid flow Reynolds number Re and the magnetic Reynolds number Rm, the Hartmann number Ha, the interaction parameter N, the injected mechanical helicity H^V and the mean dissipation rate ε. The quantities are defined by the following relationships:

$$Re = \frac{\bar{u} \cdot d_H}{\nu},\ R_m = \frac{\bar{u} \cdot d_H}{\lambda}, \qquad \text{Reynolds numbers;}$$

$$Ha = \bar{B}\, d_H \left(\frac{\sigma}{\rho \nu} \right)^{\frac{1}{2}} \qquad \text{Hartmann number,}$$

$$N = \frac{\sigma \bar{B}^2 d_H}{\rho \bar{u}} \qquad \text{Interaction parameter,}$$

$$H^V = \frac{1}{V} \int_V (\mathbf{v} \cdot (\nabla \times \mathbf{v})) dV \qquad \text{helicity (see equation 2.31)}$$

$$\varepsilon = \frac{1}{M} \sum_{i=1}^{3} \dot{V}_i \Delta p_i \qquad \text{specific dissipation}$$

Here $\bar{u}$ is the mean velocity in the helical or central channels, d_H their hydraulic diameter, $\overline{\mathbf{B}}$ a measured local mean intensity $\left|\overline{\mathbf{B}}\right|$ of the magnetic field. For $\overline{\mathbf{B}}$ we shall use the measured mean field intensity at the module centre (position $H3$). The helicity may be evaluated, if simplifying assumptions are made for the velocity distributions in the channels. We assume that a quasi rigid body rotation prevails in the helical channels and plug flow in the central channel. The angular velocity of the helical flow and the helicity of the total channel flow are then defined as

$$\Omega \approx \frac{\dot{V}_H \cdot \cos\alpha}{F_H \cdot \bar{r}} \approx \frac{\bar{u}_H}{\bar{r}} \cos\alpha\ ,\ H^V = \frac{\bar{u}_H^2}{\bar{r}} \sin 2\alpha\ , \tag{6.2}$$

where F_H is the cross-section of the helical channel, $\bar{r}$ its mean radius and α accounts for the helix pitch ($\alpha = arctg\,(h \cdot (2\pi\bar{r})^{-1})$, h – helical pitch). The total specific dissipation is evaluated using the measured volumetric flow rates $\dot{V}_i$ in the helical and central channels, the associated measured pressure losses Δp_i and the total fluid mass M contained in the channel systems. Alfvén velocities based on the measured magnetic field intensity at location $H3$ are also listed in table 1. The parameters were evaluated for experimental conditions of equal volumetric flow rates in the helical and central channels, i.e. $\dot{V}_{H1} = \dot{V}_{H2} = \dot{V}_C$, and are listed in table 1.The data of the table show that the realized volumetric flow rates correspond to high Reynolds numbers on the one side but result in low magnetic Reynolds number on the other side. In figure 5.1 the phase diagram for dynamo action is once more displayed as a function of magnetic Reynolds numbers for the helical and central flow. In the supercritical range the dynamo may be characterized by the two magnetohydrodynamic groups, the Hartmann number Ha and the Interaction parameter N. It is seen in the table that the Hartmann numbers can take on a considerable size of about $Ha = 500$ at the highest supercritical

$\dot{V}_C\,[m^3/h]$	$\dot{V}_H\,[m^3/h]$	Re_C	Re_H	$\lvert B^2\rvert\,[G^2]$	Ha_C	N	$\Omega in\,[1/s]$	$\varepsilon_{tot} = M^{-1}\sum_i \dot{V}_i \Delta p_i\,[m^2/s^3]$		$f_{in} = \frac{\Omega}{2\pi}\,[s^{-1}]$	$V_a = B(\rho\mu)^{-1/2}$ [m/s]
$\bar{u}_C\,[m/s]$	$\bar{u}_H\,[m/s]$	Rm_C	Rm_H	$\lvert B\rvert\,[G]$			$H^V = 2\Omega\,\bar{u}_{in}\sin\alpha\,[m/s^2]$	$\frac{1}{\tau} = \left(\frac{\varepsilon}{\lambda}\right)^{1/2}\,[s^{-1}]$	$L_{k\lambda} = \left(\frac{\lambda^3}{\varepsilon}\right)^{1/4}\,[m]$	$f^*_{in} = \frac{\bar{u}}{a\pi}\,[s^{-1}]$	$f = V_a(2a)^{-1}\,[s^{-1}]$ $2a = 0.42\,[m]$
115	115	6.7×10^5	4.7×10^5	2.2×10^5	590	0.55_C	37	21.7		5.9	1.37
4.1	3.1	4.03	2.83	4.7×10^2		0.73_H	82	14.7	0.082	4.7	3.3
111	111	6.5×10^5	4.2×10^5	2.15×10^5	573	0.56_C	35			5.6	1.35
3.9	3.0	3.89	2.52	4.6×10^2		0.74_H	75			4.5	3.2
106	106	6.3×10^5	4.0×10^5	2.4×10^4	187	0.07_C	33	8.23		5.25	0.44
3.8	2.8	3.75	2.39	1.5×10^2		0.09_H	66	9.1	0.105	4.2	1.04
102	102	6.0×10^5	3.8×10^5	4.5×10^2	26	$1.3\times10^{-3}{}_C$	31			4.9	0.06
3.6	2.7	3.6	2.28	2.1×10^1		$1.7\times10^{-3}{}_H$	60			4.1	0
95 (1)	95	5.6×10^5	3.3×10^5	5.0×10^2	27	$1.5\times10^{-3}{}_C$	29			4.6	0.06
3.4	2.5	3.36	2.00	2.2×10^1		$2.1\times10^{-3}{}_H$	52			3.8	0

(1) with external magnetic field $\bar{B} \approx 25\,[G]$

$P_m = \nu/\lambda \approx 6\times10^{-6}$; $d_{HC} = a/2$; $F_C = \pi/4(D_L)^2 = 0.78\times10^{-2}\,[m^2]$; $d_{HH} = \frac{h}{2(\frac{h}{a}+\frac{1}{4})} \approx \frac{2}{5}h$; $F_H = ah/4$; $\Omega = \frac{\bar{u}_{in}}{\bar{r}}\cos\alpha$; $\alpha = \text{arctg}\frac{h}{2\pi\bar{r}}$; $V_D = \lambda/(2a) = 0.25\,[ms^{-1}]$; $Ha = d_H B\left(\frac{\sigma}{\rho\nu}\right)^{1/2}$;

$N = \frac{\sigma\lvert B\rvert^2 d_H}{\rho\bar{u}_{C,H}}$

Table 1: Characteristic numbers of the Karlsruhe Dynamo experiment during operation

flow rates and still have values of $Ha = 20$ at near critical conditions. It is well known from Hartmann channel flow that the fluid dynamic velocity profile is subjected to significant deformation by Lorentz forces at Hartmann numbers of the order $Ha=20$. At Hartmann numbers of several hundred channel flow is generally strongly influenced by the Hartmann layers at the channel walls. This is certainly the case in the channel system of the dynamo module at supercritical saturated dynamo states. The significant increase in the pressure drop is an obvious sign of retardation of the velocity by Lorentz forces and dissipative Joule losses. Moreover it is to be expected that turbulent fluctuations in the high Reynolds number channel flow are strongly damped by the dynamo magnetic field according to its intensity distribution in the module. This conjecture is supported by the size of the interaction parameter N of order *one* at the higher volumetric flow rates (see section 2.5). As the interaction parameter is a measure for the ratio of the Joule dissipation time of a vortex of the size of the channel diameter and the vortex turn-around time, even the largest possible fluctuations experience a significant Joule damping. The dissipative destruction of smaller vortices is certainly stronger. Thus, a tendency to partial relaminarisation of the channel flow may be expected.

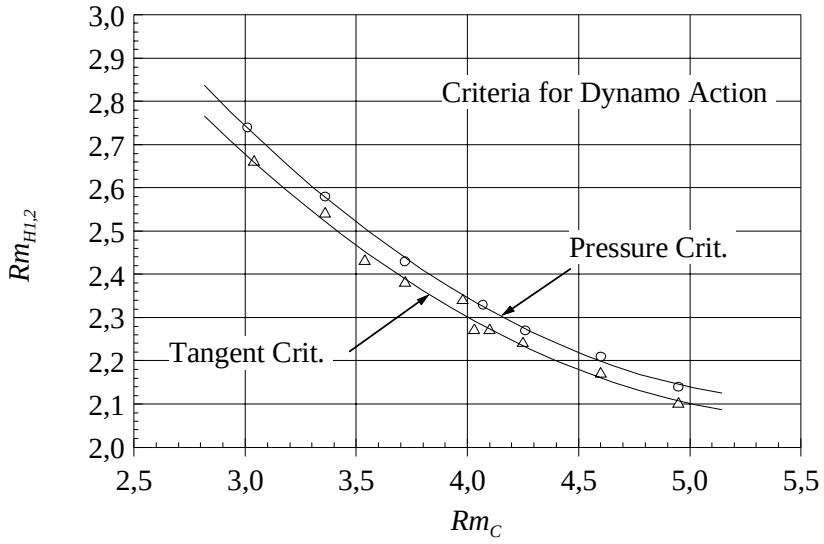

Figure 5.1: The phase diagram of the Karlsruhe dynamo experiment as a function of the helical and central Reynolds numbers Rm_H and Rm_C respectively.

The self-excitation of the dynamo has been defined in section 4.1 according to experimental criteria. These findings have been confirmed by model calculations of Tilgner (2002) and Rädler et al. (2002a). Figure 5.2 shows for comparison the experimental data and the calculated curves of Tilgner (2002) in the dynamo phase diagram. In Tilgner's calculations an effective magnetic diffusivity λ_{eff} has been used, which accounts for a correction of molecular magnetic diffusivity λ by about 10% due to turbulent motion. He also tested the sensitivity of the marginal states with regard to slight variations of the geometry of the dynamo module (the aspect ratio). The agreement between experiment and model calculation is good. Similar results have been obtained by Rädler et al. (2002a, see their figure 16).

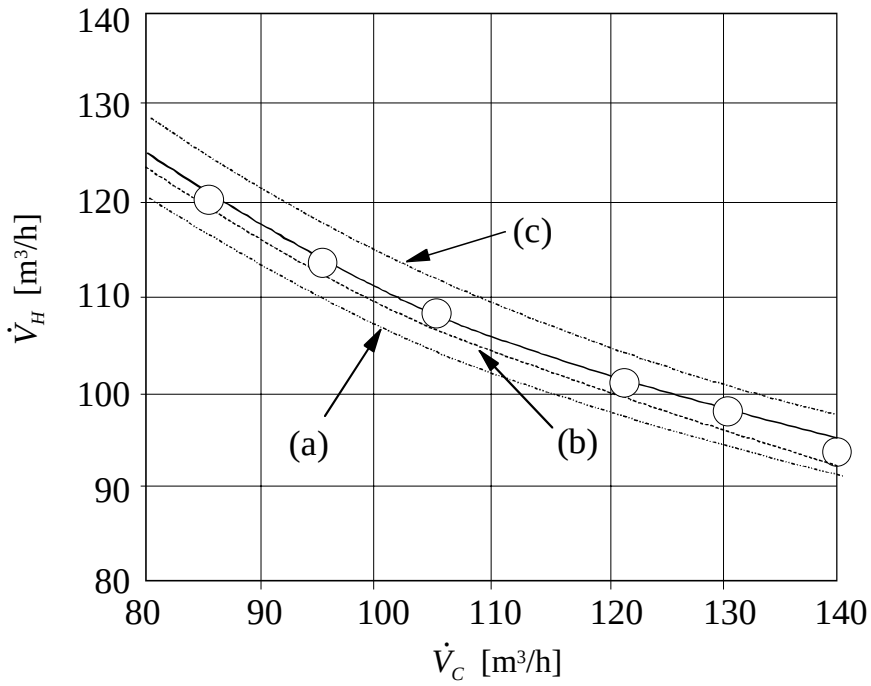

Figure 5.2: Phase diagram for dynamo action in the Karlsruhe dynamo experiment as a function of the different flow rates. Comparison between experiment and model calculations of Tilgner (2002). The continuous line corresponds to a magnetic diffusivity $\lambda=0.1 m^2/s$ *and an aspect ratio* $d/r_0=1.2$. The dashed line is for λ = 0.11m²/s and $d/r_0=1$. The dashed-dotted lines show results for $d/r_0=1$, different magnetic diffusivities $\lambda=0.11 m^2/s$ (a), $\lambda=0.115\ m^2/s$ (c) and a slightly modified velocity profile.

The overall structure of the observed magnetic field mode, as displayed in the figures 4.6 and 4.7, is in good agreement with the predictions of the model theories of Tilgner (1997, 2002) and Rädler et al. (2002). Both model theories predict a quasi-dipolar magnetic field of the mode type $m=1$ as realized in the experiment. Indeed, Tilgner & Busse (2002) calculate an isoline magnetic field which conforms with the measured isoline field of figure 4.7. There are, however, discrepancies between theoretical predictions and measurements concerning the local structure of the magnetic field. For equal helical volumetric flow rates the theory gives for positions along the cylinder axis a twisting of the radial magnetic field vectors of an angle π. The experimental measurements indicate an angle of $\pi/2$ only, as is seen from figure 4.8d. Another striking observation is the deviation of the measured distribution of the magnetic field components on the module axis. Although the measurements were taken only on the semi-axis $0 < z(mm) < 350$ there are qualitative deviations from the symmetries predicted by theory. This is seen from figure 5.3 which is a reproduction of the figure 6 of Rädler et al. (2002a) in which the experimental findings of figure 4.8a are roughly sketched. It is yet unclear, what causes this non-symmetric behaviour of the dynamo magnetic field. On the other hand, non-symmetric magnetic properties may be induced by kinematic means, i.e. by operating the test module with different helical flow rates as shown in figures 4.13a, b, c. The main effect is here the occurrence of a significant z-component of the magnetic field. It is not obvious in which way these controlled non-symmetries interfere with the inherent ones of the test module and its environment to form the actual observations.

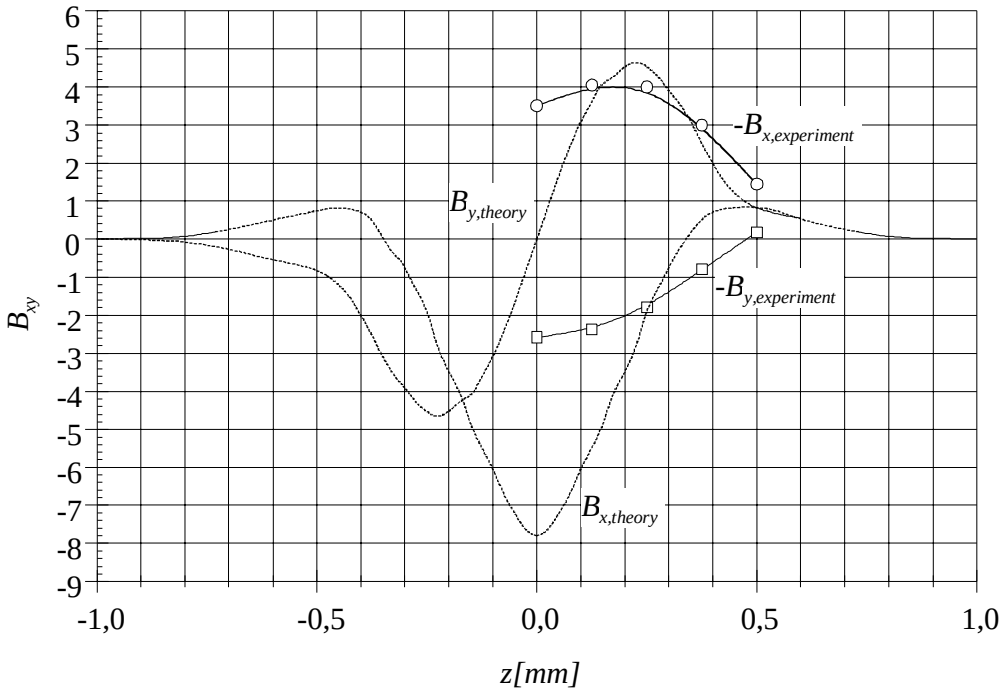

Figure 5.3: The calculated distribution of the B-field components on the module axis ($x=y=0mm$) after Rädler et al. (2002a), displayed as continuous lines for the flow rates $\dot{V}_C = \dot{V}_{H1,2} = 115m^3/h$, $\lambda = 0.1m^2/s$. The experimental results correspond to figure 4.8 and are denoted by symbols and o.

The weakly non-linear behaviour of the Karlsruhe dynamo in the supercritical regime is best characterised as an imperfect bifurcation of the magnetohydrodynamic state from a pure hydrodynamic state of helical channel flow. Although the kind of bifurcation has been identified from local field measurements only (see figures 4.9, 4.10, 4.11) one may conclude that a spatially averaged intensity of the magnetic field would show the same behaviour. The experimental results suggest that the smooth transition from the non-magnetic to a magnetic state is determined by the initial distribution of the seed field and, moreover, that this initial condition is subjected to changes depending on the intensity and duration of the action of the dynamo magnetic field on the structural environment of the test module. There is yet another permanent feature of the magnetic field generated by this test module. The intensity of the magnetic field component B_y is stronger at high supercritical conditions, if its orientation is in the negative y-direction. This again indicates a systematic structural non-symmetry of the test facility.

Tilgner and Busse (2002a) and Rädler et al. (2002b) have developed models to describe dynamo action in the slightly trans-critical regime. They find an imperfect bifurcation for the transition to dynamo action depending on the orientation of a initial seed field and thus confirm the overall observation. There is however a quantitative difference between the predicted and the measured intensities of the isolated branch. As a demonstration we reproduce here figure 9 of Rädler et al. (2002b) as figure 5.4.

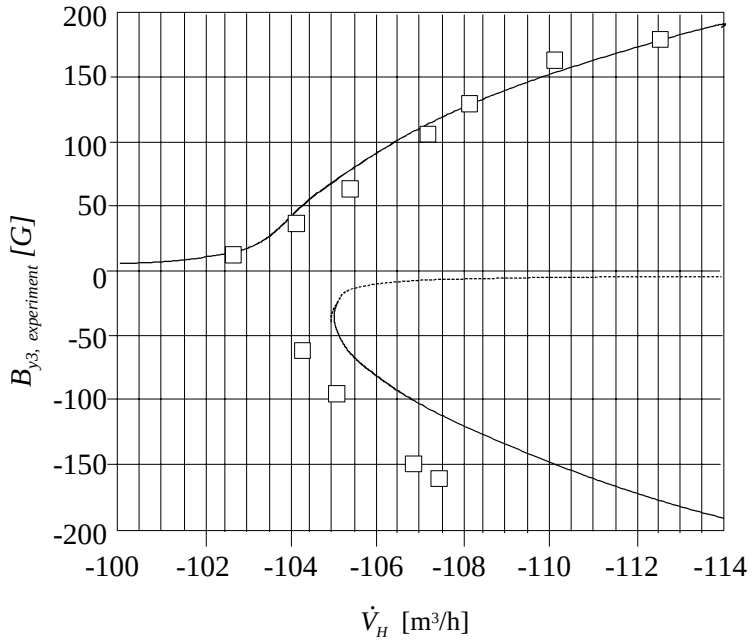

Figure 5.4: The magnetic field component B_y at the centre of the test module as a function of equal helical volumetric flow rates $\dot{V}_{H1,2}$ for a fixed central flow rate $\dot{V}_C = 112 m^3/h$. The symbol □ indicates the experimental results as presented in figure 4.10. The continuous and the dashed lines are solutions for this parameter set obtained by Rädler et al. (2002b). They employed "Mean Field" Methods in their calculations.

The experimental data correspond to those in figure 4.10. The calculations of Rädler et al. are based on a "Mean Field" approach. Tilgner & Busse (2002a) arrive at equivalent results using spectral numerical and low order analytical methods. Their results are displayed together with the data of figure 4.9 in figure 5.5. The latter procedure is briefly outlined in section 2.3. Furthermore, the model equations 2.8 and 2.9 suggest that the saturation of the magnetic field to a steady state is achieved by a reduction of the *amplification coefficient* $(\alpha - \beta|\mathbf{B}|^2)$ caused by the action of Lorentz forces which is reflected in the term $\beta|\mathbf{B}|^2$ of equation 2.8.

In general it can be stated that the theoretical predictions based on independent mathematical procedures are in fair agreement with the observations and measurements, except for certain not represented structural non-symmetries of the test module and except for some differences between the local measurements of the field intensity and the calculated values for the mean field. This is not surprising, as the calculations are based on a smoothing approximation using small scale spatial averaging.

The Gaussian character of the probability distribution of the fluctuations of the volumetric flow rate and the magnetic field components in figure 4.16 suggests that the turbulent hydromagnetic processes may be locally quasi-isotropic. This is corroborated by the vanishing skewness factor and a flatness factor of *2.5* which is close to the Gaussian value *3*. Compared to the intensity of the mean magnetic field, the intensities of the fluctuations, measured by the *RMS* value, are small of the order less than *1%* and, moreover, the relative level seems to decrease for growing mean field intensity (see figure 4.18). This indicates the higher Joule dissipative damping rates for the small scale hydromagnetic turbulence.

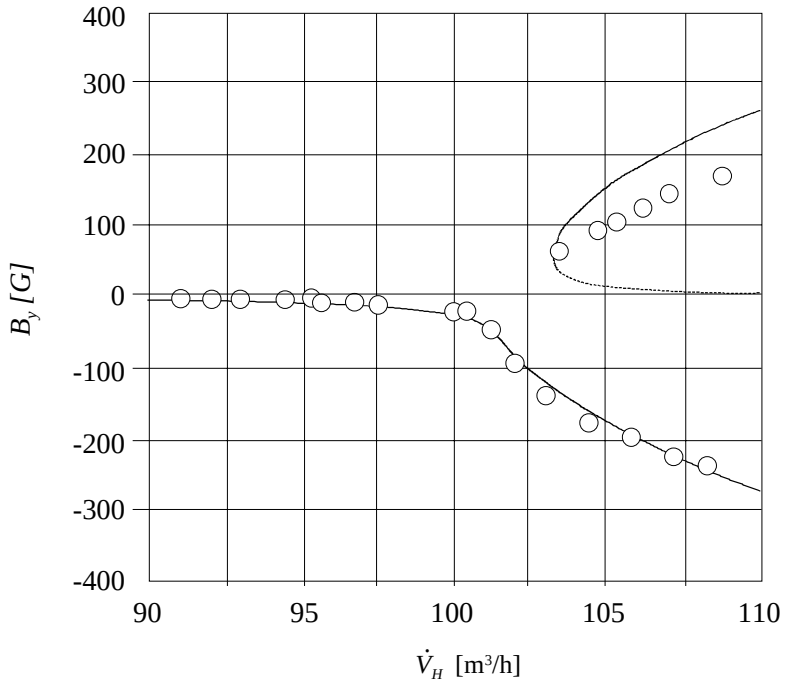

Figure 5.5: The magnetic field component B_y at the centre of the test module as a function of equal helical volumetric flow rates $\dot{V}_{H1,2}$ for a fixed central flow rate $\dot{V}_C = 112m^3/h$. The circles indicate the experimental results as presented in figure 4.9. The continuous and the dashed lines are solutions of the model equations 2.9 with Rm replaced by $\dot{V}_{H1,2}$ and $V_{crit}=102m^3/h$, $B_0=-0.5G$ and $c/\beta=9\times10^3G^2h/m^3$ according to Tilgner & Busse (2002).

The power spectra of the magnetic field fluctuations, displayed in figures 4.19-4.22 exhibit the following general features: The power level increases in the whole spectral range with increasing intensity of the local mean magnetic field. The lower frequency range $f < 0.1Hz$ in the PSD seems to approach a saturation level for the most intensive dynamo states which is particularly obvious for the B_z-component. For active dynamo states of more than about $50G$ the PSD of the B_y-components show a pronounced broad peak whose centre frequency f_p increases with the increasing intensity of the local mean magnetic field. It varies for our experimental conditions roughly in the range $1 < f(Hz) < 3$ (see figures 4.19). The other two field components do not show a similarly marked power peak. However, the B_z-component indicates a cut off frequency in the same range $1 < f(Hz) < 3$ which separates the saturated power range from the range of decaying power. The functional character of the power spectra may be discussed in the light of spectral models for magnetohydrodynamic turbulence and dynamo theory. As outlined in section 4.5 we may roughly distinguish three characteristic functional ranges in the power spectra of the B_y-component for strong dynamo action, the low frequency range $f < f_p$ with $PSD \sim f^{-1}$ behaviour, the range $f > fp$ with $PSD \sim f^{-3}$ dependence and a high frequency range $f \geq 20Hz$ with $PSD \sim f^{-5}$. There seems to exist a constant saturation level for frequencies $f < 0.1Hz$ for the most intensive dynamo states (see figure 4.19a). The functional relationships for the different ranges are suggested based on the outline of relevant spectral models for MHD-turbulence in the literature. The $PSD \sim f^{-1}$ relationship in the low frequency range seems to support the theoretical findings of Pouquet et al (1976), indicating a reverse energy cascade for a dynamo driven by a helicity injection into

the system at a particular frequency (in their terminology wave number). The spectral decay of the intensity in the frequency range $f > f_p$ may be attributed to a non dissipative forward cascading process of energy by non-local Alfvèn waves, as proposed by Grapin (1983), which would result in decay functions $PSD \sim f^{-m}$, $m > 3/2$ (see equation 2.20 and 2.21, 2.20). It may also reflect the structural reorganisation of the kinetic turbulence under the influence of the dynamo magnetic field with the side effect of significant Joule damping as suggested by Alemany et al. (1979) (see section 2.5).

The high Hartmann numbers as well as the size of the interaction parameter N of order *one* for intensive dynamo action suggests for the high frequency range that the decay is predominantly governed by Joule dissipation in Hartmann layers and in the bulk by current circuits in the free eddies of the turbulent flow. The bounding frequency f_K beyond which Joule dissipation would dominate the spectral distribution is given by the Kolmogorov Joule dissipation time scale defined in equation 2.18 in section 2.5. This is evaluated in table 1 for two cases. It varies roughly between 10 and 15 in experiments of significant dynamo action.[5] Thus, the spectral decay of the magnetic field fluctuations should vary in the frequency range $f > f_K$ between $PSD \sim f^{-11/3}$ and $PSD \sim f^{-5}$ depending on the spectral energy distribution of the turbulent velocity fields which may be of the order $E^V \sim f^{-5/3}$ or $E_r^V \sim f^{-3}$ (see equation 2.19 and 2.25 section 2.5). The experimental observation according to figures 4.19a,b,c is that there is certainly a decrease in the power for frequencies $f > 20Hz$ which may be described by rates $-5 < m < -11/3$.

It may be conjectured that the peaks in the power spectra of intensive dynamo action may correlate to the injection frequency of helicity into the dynamo module. This injection frequency is roughly defined by equation 6.2. However, the evaluation of these frequencies for the typical experiments listed in table 1 gives values between $4.2 < f_{in}(Hz) < 4.7$ (favourable evaluation). This is on the one hand a frequency range which is about twice as high as the observed frequency band of the power peaks ranging between $0.7 < f(Hz) < 3$ (cf. figure 4.19a,c) and on the other hand the experimental range of the injection frequency is considerably smaller, as its variation depends essentially on the experimentally realised volumetric flow rates. Thus, a scaling of the power peak frequency with the helicity injection frequency seems to be inadequate. A more suitable time scale for the frequency associated with the power peaks seems to be the transit time of an Alfvén wave along the structural wave lengths of the module which is $L=2a$. The corresponding frequency scale is $f_A \approx V_a / 2a$. In table 1 these frequencies are evaluated for three relevant cases. The frequencies of the power peaks in the spectra agree fairly well with the reciprocal transit times of the Alfvén waves along the characteristic structural length scale. An equivalent result has been obtained by evaluating the location of power peaks in figure 4.19c. It may therefore be conjectured that the power peaks in the power density spectra reflect a resonant interaction of Alfvén waves with wave lengths comparable to the small structural length scale *a* of the module. This conjecture is supported by the cross-correlation measurements (see figures 4.22, 4.23) which show that the high frequency signals are strongly correlated at short distances of

[5] The corresponding Kolmogorov length scale has also been evaluated for the considered cases. It varies in the range $0{,}08 – 0{,}105m$ and is thus of the order of the hydraulic diameters of the channels of the vortex generators (see Table 1).

tances of two Hall probes, but are uncorrelated at distances of the module's dimension. Moreover, the correlation function for the high frequency signals indicate a delay time, while the low frequency correlations for large distances of the probes do not. This is not surprising in the light of the theory or Alfvén waves as outlined in section 2.4. Even for the most intensive dynamo actions in our experiments Alfvén waves are dampened in liquid sodium on length scales of about 0.1 to $0.4\ m$. [6]

[6] It may be questioned, whether the oscillatory features of the magnetic field should be associated to the phenomena of linear Alfven wave propagation, as these waves are strongly dampened in liquid sodium. However, at supercritical conditions there is the possibility of non-linear interactions of dampened waves which may lead to sustained finite amplitude waves. In this context Grapin et al.(1983) speak of 'Alfvenic fluctuations'.

6 Conclusions and perspectives

The Karlsruhe dynamo experiment has demonstrated that a permanent magnetic field of considerable intensity can be spontaneously generated by a regular arrangement of stationary vortices in a conducting fluid. The saturation of the magnetic field is achieved by the feed back of the magnetic field on the velocity distribution. This is suggested by the dynamo model of Tilgner & Busse (2002) as well as that of Rädler et al. (2002b) which are well supported by the experimental findings. Another characteristic property of the dynamo magnetic field are the turbulent fluctuations of the field intensity about its mean value. Although it may be conjectured that these fluctuations correlate with the velocity fluctuations of the turbulent channel flow, direct measurements could not yet be performed, as velocity measurements, in particular velocity fluctuation measurements, in liquid metal flow are difficult and tedious. Further experiments with an adequate instrumentation for velocity measurements should corroborate this conjecture and also confirm the feedback of the dynamo magnetic field on the mean velocity.

There is yet another deficiency concerning the magnetic field measurements. The Hall probes provide only information on the local field intensity. For the overall assessment of the generated magnetic energy an integral measurement of the magnetic field would be more appropriate. Three induction coils penetrating the dynamo axis and closing along the cylinder mantle could provide valuable integral information about field transients and oscillations. However, because of technical difficulties in eliminating uncontrolled perturbations the time signals have not yet been evaluated properly. In a forthcoming experiment this instrumentation will have to be improved and utilised.

The Karlsruhe test facility bears another challenge. It is to realize a second mode of possible non-symmetric dynamo field solutions. The axis of this quasi-dipole field would be oriented vertically and perpendicular to the cylinder axis of the module. This mode has been predicted by Tilgner (1998). It is intended to initiate this dynamo mode by a properly shaped initial seed magnetic field in another dynamo test campaign.

7 Acknowledgements

The Karlsruhe dynamo experiment could not have been performed without the continuous support of this project by the executive board of the Forschungszentrum Karlsruhe. The authors gratefully acknowledge this support. They greatly thank the staff of the central workshop of the Forschungszentrum for their excellence in constructing the test module. In particular they like to thank the technical staff of the Institut für Kern- und Energietechnik, E. Arbogast, V. Krieger, W. Liebel, K. Marten, J. Meinel, P. Miodek, F. K. Nikolaus, D. Rackel, D. Schlindwein.

They are indebted to their colleagues, L. Barleon, L. Bühler, H. Hofmann, J. Reimann for fruitful discussions and technical assistance.

Theoretical input to the experimental dynamo program was continuously provided by F. Busse and A. Tilgner of the University of Bayreuth and K. H. Rädler and his colleagues of the Astrophysikalisches Institut Potsdam. Their theoretical support has been extremely valuable for the success of the experiment.

The members of the Karlsruhe Dynamo Project Council, W. Deinzer from the University of Göttingen, M. Proctor from the University of Cambridge, UK, K. H. Rädler from the Astrophysikalisches Institut Potsdam, M. Stix from the Kiepenheuer Institut für Sonnenphysik in Freiburg deserve our special thanks for their positive valuation of the experimental program and their constructive comments during the early phase of the research project.

Finally, the authors thank the Deutsche Forschungsgemeinschaft for a financial support of Sandor Horanyi for his evaluation of the large experimental data sets.

8 References

Alemany A., Moreau R., Sulem P.L., Frisch U., 1979:
Influence of an external magnetic field on homogeneous MHD turbulence, Journal de Mécanique Vol. 18, pp. 277-313.

Rädler K.-H., Apel A., Apstein E., Rheinhardt M., 1996:
Contributions to the theory of the planed Karlsruhe dynamo experiment; AIP-Report, July 1996.

Biskamp D. , 1993:
Nonlinear Magnetohydrodynamics; Cambridge University Press.

Busse F. H., Carrigan C. R., 1976:
Laboratory Simulation of Thermal Convection in Rotating Planets and Stars; Science 191, 81-93.

Busse F. H., 2000:
Homogeneous Dynamos in Planetary Cores and in the Laboratory; Ann. Rev. Fluid Mech. 2000, 32, pp. 838-308.

Busse F. H., 1971:
Motions within the Earth's Core; Zeitschr. Geophys. 37, pp. 153-177.

Busse F. H., 1971:
Bewegungen im Kern der Erde; Zeitschrift für Geophysik 37, pp. 153-177.

Busse F. H., 1978:
Magnetohydrodynamics of the Earth's dynamo; Ann. Rev. Fluid Mech. 10, pp. 435-462.

Busse F. H., 1992:
Dynamo Theory of Planetary Magnetism and Laboratory Experiments. In: Springer Proceedings in Physics 69; Evaluation of Dynamical Structures in Complex Systems, Eds. R. Friedrich, A. Wunderlin, Springer pp. 197-207.

Busse F. H., 1994:
Convection driven zonal flows and vortices in the major planets; Chaos 4, pp. 123-134.

Busse F. H., Carrigan C. R., 1974:
Convection induced by centrifugal buoyancy; J. Fluid Mech. 62, pp. 579-592.

Carrigan C. R., Busse F. H., 1983:
An experimental and theoretical investigation of the onset of convection in rotating spherical shells; J. Fluid Mech. 126, pp. 287-305.

Childress S., 1967:
A class of solutions of the magnetohydrodynamic dynamo problem.
In: The application of modern physics to the Earth and planetary interiors;
Proc. NATO Adv. Study Inst. Newcastle, April 1967, ed. S. K. Runcorn,
Wiley-Interscience

Childress S:, 1970:
New Solutions of the kinematic dynamo problem;
J. Math. Phys. 11, pp. 3063-76.23-29.

Davidson P.A., 2001:
An Introduction to Magnetohydrodynamics; Cambridge University Press.

Frisch U. , Pouquet A., Leorat J., Mazure A. ,1975:
Possibility of an inverse cascade of magnetic helicity in magnetohydrodynamic turbulence; J. Fluid Mech. 68, pp. 769-778.

Gailitis A., 1967:
Self-excitation conditions for a laboratory model of a geomagnetic dynamo; Magnetohydro-dynamics 3, pp.23-29.

Gailitis A. , Lielausis O. , Dement'ev S. , Platacis E. , Cifersons A. , Gerbeth G. , Gundrum Th. , Stefani F. , Cristensen M. , Haenel H. , Will G. , 2001:
Magnetic Field saturation in the Riga Dynamo Experiment; Phys. Rev. Letters 86, pp 3024-3027.

Glatzmaier G. A., Roberts P. H. 2000:
Geodynamo theory and simulations; Reviews of Modern Physics 72, 1081-1123.

Golubitzky M., Schaefer G. D. , 1985:
Singularities and Groups in Bifurcation Theory; Springer, New York, Berlin

Grappin R. , Pouquet A. , Leorat J. 1983 :
Dependence of MHD-turbulence spectra on the velocity-magnetic field correlation; Astron. Astrophys. 126, pp. 51- 58.

Hinze J. O., 1975:
Turbulence; McGraw-Hill 1975

Irishnikov P. S., 1964:
Turbulence of a conducting fluid in a strong magnetic field; Sov. Astron. 7, pp. 566-571.

Jones C.A.,2000:
Convection-driven geodynamo models; Phil. Trans. R. Soc. London, A 358, pp.873-897.

Joos G., Joseph D. D., 1980:
Elementary Stability and Bifurcation Theory; Springer

Kolmogorov A. N., 1941:
Local structure of turbulence in an incompressible fluid at large Reynolds numbers; Dokl. Akad. Nauk. SSSR 30, pp. 299-303.

Kraichnan R. H., 1965:
Inertial range spectrum in hydromagnetic turbulence; Phys. of Fluids 8, pp. 1385- 1387.

Leorat J., Pouquet A. , Frisch U., 1981:
Fully developed MHD-turbulence near critical magnetic Reynolds numbers ; J. Fluid Mech. 104, pp. 419-443.

Moss D., 1997:
Dynamo generation of cosmic magnetic fields; Contemp. Phys. 18, pp. 49-62.

Müller U., Stieglitz R., 2002:
The Geodynamo: Models and Supporting Experiments; Reviews in Geophysics, submitted 2002.

Pekeris C.L., Accad Y. Shkoller B., 1973:
Kinematic Dynamos and the Earth's Magnetic Field; Phil. Trans. R. Soc. Lond. A275, pp.425-461.

Pouqet J., Frisch U., Leorat J., 1976:
Strong MHD helical turbulence and the nonlinear dynamo effect; J. Fluid Mech. 77, pp. 321-354.

Rädler, K.-H., 1995:
Cosmic Dynamos; Review in Modern Astronomy 8, pp.295-321.

Rädler K.-H., Apstein E., Rheinhardt M., Schüler M., 1998:
The Karlsruhe Dynamo Experiment, a Mean Field Approach; Studia geophys. et. geod. 42, pp. 320-327.

Rädler K.-H., Rheinhardt M., Apstein E., Fuchs H., 2002a:
On the mean-field theory of the Karlsruhe dynamo experiment. 1. Kinematic theory ; Magnetohydrodynamics 38, pp. 41-71.

Rädler K.-H., Rheinhardt M., Apstein E., Fuchs H., 2002b:
On the mean-field theory of the Karlsruhe dynamo experiment. 2. Back-reaction of the magnetic field on the fluid flow; Magnetohydrodynamics 38, pp.73-94.

Rittinghouse Inglis D., 1981:
Dynamo theory of the Earth's varying magnetic field; Reviews of Modern Physics 53, pp. 481-496.

Roberts G.O., 1970:
Spatially periodic dynamos; Phil. Trans. R. Soc. London A266, 535-558.

Roberts G.O., 1972:
Dynamo Action of Fluid Motions with Two-dimensional Periodicity; Phil. Trans. R. Soc. London A. 271, pp. 411-453.

Stieglitz R. , Müller U. , 1996:
GEODYNAMO- Eine Versuchsanlage zum Nachweis des homogenen Dynamoeffekts; Wissenschaftliche Berichte FZKA 5716.

Stieglitz R. , Müller U. , 2001:
Experimental demonstration of the homogeneous two-scale dynamo; Phys. Fluids 13, pp.561-564.

Tennekes H., Lumley J. L. , 1977: A First Course in Turbulence; MIT Press.

Tilgner A., Busse F., 2002:
Simulation of the bifurcation diagram of the Karlsruhe dynamo, Magnetohydrodynamics 38, pp. 35-40.

Tilgner A. , 2002:
Numerical simulation of the onset of dynamo action in an experimental two-scale dynamo; submitted for publication in Phys. Fluids.

Tilgner A., 1997:
A kinematic dynamo with a small scale velocity field; Physics Letters A226, pp. 75-79.

Zhang K., 1992:
Spiralling columnar convection in rapidly rotating spherical shells; J. Fluid Mech. 236, pp. 535-556.

9 Appendix A.1 Figure Captions

Figure 2.1 Columnar vortex pattern of buoyancy driven convection in a rapidly rotating spherical shell after Busse (1994).

Figure 2.2: a) Non-confined periodic vortex pattern after Roberts (1972) and in modified form after Busse (1992); b) Busse's vortex arrangement confined in a cylindrical domain; c) Tilgner's (1997) and Apel et al. (1996) vortex arrangement in a sphere.

Figure 2.3: The bifurcation diagram for the Karlsruhe Dynamo experiment calculated by Tilgner & Busse (2002) for equal volumetric flow rates.

Figure 3.1: Semi-technical sketch of the Karlsruhe dynamo test module. a) internal structure and velocity distribution; b) vortex generator; c) technical design.

Figure 3.2: Sketch of the locations of the Hall sensors in the test module at location $H3$: two Hall sensors to measure three field components B_x, B_y, B_z; location $H4$: one Hall sensor to measure B_y; location $H5$: one Hall sensor to measure two components B_z and B_r i.e. the radial component; location $H6$: one Hall sensor to measure the radial component B_r.

Figure 3.3: The distribution of the seed magnetic field along the module axis in the range $0 \le z(mm) \le 350$ recorded at the beginning and the end of a measuring campaign. There is a noticeable change in the local characteristic of the seed field. Volumetric flow rates $\dot{V}_C = \dot{V}_{H1,2} = 0 m^3/h$; $\lambda = 0.1 m^2/s$.

Figure 4.1 Time signal recordings for a) volumetric flow rates; b) pressure losses in the helical and central channels; c-d) magnetic field components for an experimental operation with stepwise changing flow rates.

Figure 4.2: Magnetic field components B_x and B_y for saturated steady dynamostates for a constant central flow rate $\dot{V}_C = 85 m^3/h$ and variable helical flow rates $110 < \dot{V}_{H1,2} (m^3/h) < 130$.

Figure 4.3: Pressure losses in the helical and central piping systems of the test module under steady state operation conditions for a) $\dot{V}_C = 85\ m^3/h$, $110 < \dot{V}_{H1,2} (m^3/h) < 130$; b) $\dot{V}_C = 105\ m^3/h$, $80 < \dot{V}_{H1,2} (m^3/h) < 120$.

Figure 4.4: The state diagram for dynamo action for the Karlsruhe test module, □ pressure loss criterium; o tangent criterium.

Figure 4.5: Isoline surface of the y-components of the magnetic field measured in the centre of the module depending on the helical and central volumetric flow rates $\dot{V}_C$ and $\dot{V}_{H1,2}$.

Figure 4.6: a.) Array of compass needles arranged on vertical wood boards sidewise of the test module and parallel to its axis; b.) in front of the module and perpendicular to its axis. Experimental conditions: $\dot{V}_C = 134m^3/h$, $\dot{V}_{H1,2} = 101m^3/h$ and $\lambda = 0.1m^2/s$.

Figure 4.7: Isolines of the normal components of the magnetic field measured in the plane of the side wise arranged vertical wood board for the conditions $\dot{V}_C = 134m^3/h$, $\dot{V}_{H1,2} = 101m^3/h$ and $\lambda = 0.1m^2/s$.

Figure 4.8: Distribution of the intensities of the magnetic field components on the module axis in the range $0mm \le z \le 350mm$ for equal volumetric flow rate: a) $\dot{V}_H = \dot{V}_C = 115\ m^3/h$; b) $\dot{V}_H = \dot{V}_C = 110m^3/h$; variation of the angle of inclination of the magnetic field relative to the module's position for c) $\dot{V}_H = \dot{V}_C = 115m^3/h$; d) $\dot{V}_H = \dot{V}_C = 110m^3/h$.

Figure 4.9: The stationary dynamo states at supercritical conditions represented by the measured local B_y-component. The graph shows two sequences of stationary states, one set on a continuous branch and another set on an isolated branch. The return jump from the isolated branch to the continuous branch is indicated by the symbol ◄. Parameter range: $\dot{V}_C = 112\ m^3/h$, $92 < \dot{V}_{H1,2}\,(m^3/h) < 110$.

Figure 4.10: Stationary dynamo states on a continuous and an isolated branch of a bifurcation graph, however, compared to figure 4.9 the branches are reversed due to a modification of the environmental seed magnetic field by the dynamo magnetic field of the preceding experiment. Parameter range: $\dot{V}_C = 112\ m^3/h$, $98 < \dot{V}_{H1,2}\,(m^3/h) < 113$.

Figure 4.11: Stationary dynamo states continuously connected to hydrodynamic states for both directions of the magnetic field. The states were obtained in a monotonic up- and down-scan with a switch over to the other branch at high magnetic field intensities. It is suggested that the change of the field direction at high field intensity modifies the environmental seed field by changing the remanent week ferromagnetism in the steel structures of the laboratory building. Parameter range: $\dot{V}_C = 115m^3/h$, $89 < \dot{V}_{H1,2}\,(m^3/h) < 130$.

Figure 4.12: The measured seed magnetic field at low sub-critical volumetric flow rates $\dot{V}_H = \dot{V}_c = 77.5m^3/h$ before (a) and after (b) a measuring campaign with dynamo action of high intensity i.e. $|B| \sim 0(400\ G)$.

Figure 4.13: Distribution of the magnetic field components along the axis of the module in the range $0 \le z \le 350mm$ for symmetric and non-symmetric flow distributions. (a) $\dot{V}_{H1} = \dot{V}_{H2} = 100m^3/h, \dot{V}_C = 128m^3/h$; (b) $\dot{V}_{H1} = 85m^3/h$, $\dot{V}_{H2} = 115m^3/h$, $\dot{V}_C = 128m^3/h$; (c) $\dot{V}_{H1} = 115m^3/h$, $\dot{V}_{H2} = 85m^3/h$, $\dot{V}_C = 128m^3/h$. Legend: $\Delta \rightarrow B_x$, $\square \rightarrow B_y$, $o \rightarrow B_z$.

Figure 4.14: Touples of volumetric flow rates of long time signal recording experiments.

Figure 4.15: Typical time signals of the volumetric flow rate and two components of the magnetic field (B_y, B_z) of the Hall-probe *H3* for constant volumetric flow rates $\dot{V}_C = \dot{V}_{H1,2} = 115m^3/h$ at $z=0$. (a) time interval *20s*; (b) time interval *2s*.

Figure 4.16: Probability density function (*PDF*) of the time signals of the volumetric flow rate and the two components of the magnetic field (B_y, B_z) of the Hall-probe *H3* for constant volumetric flow rates $\dot{V}_C = \dot{V}_{H1,2} = 115m^3/h$ at $z=0$.

Figure 4.17: The square root of the variance (RMS), skewness and flatness values of time signal $B_y(0,0,0,t)$ of Hall-Probe *H3* at $z=0$ for the flow rates $\dot{V}_C = \dot{V}_{H1,2} = 115m^3/h$.

Figure 4.18: The square root of the variance (*RMS*) values and the associated mean values for the time signals of B_x, B_y, B_z as a function of the flow rates. (a) *RMS*-values; (b) the associated mean values.

Figure 4.19: Power spectral density (*PSD*) for the components B_x, B_y, B_z for five different volumetric flow rates of operation at the position $z=0$ of Hall-probe *H3*. (a) *PSD* for the B_y-component for five equal volumetric flow rates $\dot{V} = 95, 102, 106, 111$ and $115m^3/h$; (b) *PSD* for the B_z-component for five equal volumetric flow rates $\dot{V} = 95, 102, 106, 111$ and $115m^3/h$; (c) *PSD* for B_y-component for $\dot{V}_{H1} = \dot{V}_{H2} = 100m^3/h$ and for five central volumetric flow rates $\dot{V}_C = 106, 116, 120, 125$, and $136m^3/h$.

Figure 4.20: Power spectral density *(PSD)* for the components B_x, B_y, B_z for two different volumetric flow rates of operation. (a) $\dot{V}_C = 105m^3/h$, $\dot{V}_{H1,2} = 120m^3/h$; (b) $\dot{V}_C = 115m^3/h$, $\dot{V}_{H1,2} = 105m^3/h$.

Figure 4.21: Power spectral density (*PSD*) of the components B_y, B_x, B_z of Hall-probe *H3* for volumetric flow rates $\dot{V}_C = \dot{V}_{H1,2} = 115m^3/h$ and at the positions $\vec{X} = (0, 0, 0mm)$, $\mathbf{X} = (0, 0, 87.5mm)$, $\mathbf{X} = (0,0,175\ mm)$, $\mathbf{X} = (0, 0, 350\ mm)$. (a) B_y ; (b) B_x and (c) B_z.

Figure 4.22: Cross-correlation function (*CCF*) obtained from B_y-recordings of Hall probes *H3* and *H4* at different positions on the module axis in the range $-135 < z_{H4}(mm) < 365$, $0 < z_{H3}(mm) < 350$; displayed time intervals. (a) $-200 < \tau(s) < 200$; (b) $-20 < \tau(s) < 20$; (c) $-5 < \tau(s) < 5$. Experimental condition: $\dot{V}_C = \dot{V}_{H1,2} = 115m^3/h$, $\lambda = 0.1m^2/s$.

Figure 4.23: Cross-correlation function (*CCF*) obtained from signal recordings of Hall probes at positions *H3* and *H6*. Experimental condition: $\dot{V}_C = \dot{V}_{H1,2} = 115m^3/h$, $\lambda = 0.1m^2/s$.

Figure 5.1: The phase diagram of the Karlsruhe dynamo experiment as a function of the helical and central Reynolds numbers Rm_H and Rm_C respectively.

Figure 5.2: Phase diagram for dynamo action in the Karlsruhe dynamo experiment as a function of the different flow rates. Comparison between experiment and model calculations of Tilgner (2002). The continuous line corresponds to a magnetic diffusivity $\lambda=0.1m^2/s$ *and an aspect ratio* $d/r_0=1.2$. The dashed line is for λ = 0.11m^2/s and d/r$_0$=1. The dashed-dotted lines show results for d/r$_0$=1, different magnetic diffusivities $\lambda=0.11m^2/s$ (a), $\lambda=0.115\ m^2/s$ (c) and a slightly modified velocity profile.

Figure 5.3: The calculated distribution of the B-field components on the module axis ($x=y=0mm$) after Rädler et al. (2002), displayed as continuous lines for the flow rates $\dot{V}_C=\dot{V}_{H1,2}=115m^3/h$, $\lambda=0.1m^2/s$. The experimental results correspond to figure 4.8 and are denoted by symbols and o.

Figure 5.4: The magnetic field component B_y at the centre of the test module as a function of the helical volumetric flow rate $\dot{V}_{H1,2}$ for a fixed central flow rate $\dot{V}_C=112m^3/h$. The symbol □ indicates the experimental results as presented in figure 4.10. The continuous and the dashed lines are solutions for this parameter set obtained by Rädler et al. (2002). They employed higher order "Mean Field" Methods in their calculations.

Figure 5.5: The magnetic field component B_y at the centre of the test module as a function of the helical volumetric flow rate $\dot{V}_{H1,2}$ for a fixed central flow rate $\dot{V}_C=112m^3/h$. The circles indicate the experimental results as presented in figure 4.9. The continuous and the dashed lines are solutions of the model equations 2.9 with Rm replaced by $\dot{V}_{H1,2}$ and $V_{crii}=102m^3/h$, $B_0=-0.5G$ and $c/\beta=9\times10^3G^2h/m^3$ according to Tilgner & Busse (2002)